



Advancing the precision of thermal Hall measurements for novel materials research

Danny Kojda^{a,*}, Ida Sigusch^{a,b}, Bastian Klemke^a, Sebastian Gerischer^a, Klaus Kiefer^a, Katharina Fritsch^a, Christo Gugushev^c, Klaus Habicht^{a,b}

^a Helmholtz-Zentrum Berlin für Materialien und Energie GmbH, Hahn-Meitner-Platz 1, Berlin, D-14109, Germany

^b Institute of Physics and Astronomy, University of Potsdam, Karl-Liebknecht-Straße 24-25, Potsdam, D-14476, Germany

^c Leibniz-Institut für Kristallzüchtung, Max-Born-Straße 2, Berlin, D-12489, Germany

ARTICLE INFO

Keywords:

Thermal Hall effect
Terbium titanate
Capacitance thermometry

ABSTRACT

Precision thermal Hall measurements unlock potential for unraveling fundamental thermal transport principles in novel materials. This work addresses the challenge of resolving sub-mK temperature differences in magnetic fields by employing high-precision capacitance thermometry with thermalized electronics, achieving a background noise of approximately 40 μ K at 30 K. The novelty lies in the improvement and combination of innovative approaches, including the application of attenuators for thermal anchoring, a modular multi-stage approach to reduce thermal gradients, direct thermometer-sample assembly, and the use of individual capacitance bridges for faster measurements. The setup performance is demonstrated for the pyrochlore oxide terbium titanate and the longitudinal and transverse thermal conductivities agree with the literature. We show that the transverse temperature difference is proportional to the product of magnetic field times heating power for fields up to 5 T, enabling improved statistics compared to individual sweeps analysis. We conduct an analysis of uncertainties in the transverse thermal conductivity, considering various thermometer calibrations for extracting temperature differences. This analysis reveals a significant influence of the longitudinal conductivity on the transverse thermal conductivity. These advancements allow for unprecedented temperature resolution and stability, while identified resolution limitations pave the way for next-generation setups.

1. Introduction

Thermal Hall conductivity measurements have attracted large attention recently because of their key role in identifying novel excitations, quasiparticles with unusual properties and new phases in condensed matter. Accessing the transverse thermal conductivity provides a valuable tool to separate these exotic excitations from conventional phonon dynamics and to study topologically non-trivial phases of bosonic systems which are otherwise notoriously difficult to discern from their trivial counterparts by other methods. The thermal Hall effect (THE) is observed in a broad range of materials including spin liquids [1], spin-ice [2] materials, parent phases of high- T_C superconductors [3] and materials with strongly polar properties [4].

A prominent THE example is the quantum spin-liquid phase of two-dimensional honeycomb structures, amenable to an exact solution by the Kitaev model and characterized by the emergence of fractionalized Majorana fermion excitations [5]. Experimentally, a plateau with half-

integer quantization was observed in the thermal Hall conductivity in α - RuCl_3 . This has been interpreted as a signature of edge currents carried by Majorana fermions and is presently discussed in literature [6–11].

The THE in Mott insulators informs about mechanisms responsible for the chirality of phonons [12] being the dominant heat carriers, e.g. in cuprates Nd_2CuO_4 and $\text{Sr}_2\text{CuO}_2\text{Cl}_2$.

Recently, the phonon THE in quantum paraelectric materials has been discovered in bulk SrTiO_3 [4]. Similar to SrTiO_3 , black phosphorus exhibits phonons as the only collective excitations, with a transverse thermal Hall conductivity that exceeds values previously reported in any other insulator [13]. Despite intense experimental [14,15] and theoretical efforts [16–19], the origin of this effect remains elusive, calling for further investigations.

Signatures of topological phase transitions in the transverse thermal Hall conductivity produced by magnons in collinear antiferromagnetic insulators on a honeycomb lattice have been theoretically predicted [20] and a tunable magnonic thermal Hall effect in skyrmion-

* Corresponding author.

E-mail address: danny.kojda+MD@gmail.com (D. Kojda).

textured crystal phases of ferrimagnets has been theoretically studied [21], both awaiting experimental confirmation in candidate materials. The aforementioned examples clearly demonstrate the tremendous importance of thermal Hall experiments for current and future fundamental research and prospective applications.

The formidable challenge for successful THE experiments is posed by the small order of magnitude of the transverse Hall signals. Typically, the thermal Hall conductivity is in the order of 1×10^{-3} to $1 \times 10^{-4} \text{ WK}^{-1} \text{ m}^{-1}$ for magnetic fields in the range of a few Tesla [12, 22]. A reliable detection of transverse Hall signals therefore requires the precise measurement of temperature differences in the sub-mK range for typical millimeter-sized samples. Minimization of parasitic heat-transfer paths, together with long-term temperature stability, in combination with long-term stability of the temperature sensing electronics is necessary preconditions to extract intrinsic THEs of investigated samples. Residual measurement errors induced by geometrical uncertainties or magnetic-field dependencies, among other causes responsible for finite signal offsets, additionally require correction strategies such as anti-symmetrization. In addition to high-precision thermometry, high-quality crystal samples are also required to minimize signals superimposing the intrinsic effects, e.g. signals arising from skew scattering of the heat carriers by crystal imperfections such as point defects, dislocations or grain boundaries.

Over the last years, several groups have developed thermal Hall instrumentation and employed different experimental solutions to address the extreme challenges of detecting a small transverse thermal conductivity. Regarding precise temperature sensing, three distinct experimental realizations have been pursued with state-of-the-art instrumentation: resistive [23], thermoelectric [13,24] and capacitive [25,26] thermometry. Because the first two are prone to the influence by magnetic field effects extensive calibration is required as function of each applied field and temperature. Presently, such resistive thermometers can be purchased with high quality and calibrated from commercial suppliers and are the standard solution for temperatures down to $\sim 0.1 \text{ K}$. The latter, capacitive thermometry, is significantly less sensitive to magnetic fields and does intrinsically not dissipate any power. It is advantageous that the dielectric material used exhibits a strongly temperature-dependent permittivity in the temperature range of interest and parasitic capacitances in the measurement circuits can be overcome. The signal processing hardware and the readout electronics depend on the specific thermometry and must satisfy the requirements for high resolution, low noise and minimal parasitic signals. A previous study included a direct comparison of the applicability of different thermometer types for the THE and provides a field-dependent calibration of a Cernox sensor [27].

Here, we report the performance of thermal Hall instrumentation based on capacitive thermometry. This setup is able to resolve sub-mK temperature differences. After a brief introduction to the theoretical aspects of the thermal Hall effect, we describe in detail the design of a stand-alone sample stick with a modular design which can be easily inserted into various cryomagnets with vertical magnetic field geometry. Special attention is given to the thermalization of the experimental stages and their temperature regulation. An outline of the temperature signal paths is given alongside a description of the readout electronics based on capacitance bridges. Different experimental protocols have been developed in terms of calibration and measurement sequences with respect to signal anti-symmetrization which is vital to extract correct transverse thermal conductivity. Besides drift corrections, our data processing workflow entails offset corrections by standard anti-symmetrization procedures. We show that the thermal Hall conductivity can be reliably extracted from the linear dependence of the Hall signal on $B \cdot P$, i.e. the product of magnetic field B and heater power P at moderate magnetic fields up to 5 T. The overall performance of our thermal Hall instrumentation is evaluated by measurements on a high-quality sample of $\text{Tb}_2\text{Ti}_2\text{O}_7$, demonstrating excellent temperature resolution well below $100 \mu\text{K}$ at 30 K .

Generally, high resolution in ΔT_y is desired for uncovering subtle effects that may be obscured at lower resolution. On the other hand, lower values of $B \cdot P$ offer the advantage that temperature gradient through the sample can be smaller. The lower $B \cdot P$ also contribute to enhanced sustainability and accessibility, particularly benefiting groups working with cryogenic magnets of limited field, considering the high operating costs and resource efforts associated with high-field magnets.

2. Determination of thermal conductivity

From a theoretical point of view, the thermal conductivity tensor is derived from the current-current correlation function within linear response theory and a Green-Kubo formalism adapted to the temperature gradient taking the role of a generalized external force [28]. As opposed to the semiclassical Boltzmann transport equation, Green-Kubo theory relies on a proper quantum mechanical approach and allows for the derivation of transverse and longitudinal thermal conductivities from a given model Hamiltonian.

From an experimental point of view, the longitudinal current density j_x is defined by the heater power P per unit cross-sectional area of the sample $A = L_y L_z$, with L_y and L_z denoting the sample width and height, respectively. It is related to the thermal conductivity tensor κ by Fourier's law, which for a two-dimensional system reads

$$\begin{pmatrix} j_x \\ j_y \end{pmatrix} = \begin{pmatrix} \kappa_{xx} & \kappa_{xy} \\ -\kappa_{yx} & \kappa_{yy} \end{pmatrix} \begin{pmatrix} \partial_x T \\ \partial_y T \end{pmatrix}. \quad (1)$$

In the experiment, we assume the longitudinal thermal conductivity to be isotropic by $\kappa_{xx} = \kappa_{yy}$. It is important to note that time-reversal symmetry dictates the thermal conductivity tensor to be symmetric, as stated by the Onsager relations, which implies that the transverse thermal conductivity has odd symmetry with respect to magnetic field reversal and $\kappa_{xy} = -\kappa_{yx}$. Further, we take into account that the transverse current density $j_y = 0$ is defined to be zero by experiment, since nominally no thermal current is allowed to flow in the transverse direction in the standard thermal Hall configuration. Assuming constant temperature gradients across the sample, i.e. $\partial_x T = -\Delta T_x / \Delta L_x$ and $\partial_y T = -\Delta T_y / \Delta L_y$, we obtain for materials in which the transverse thermal conductivity is much less than the longitudinal thermal conductivity $\kappa_{xy} \ll \kappa_{xx}$:

$$\kappa_{xx} = \frac{P \Delta L_x}{\Delta T_x \Delta L_y L_z}, \quad (2)$$

$$\kappa_{xy} = \kappa_{xx}^2 \frac{\Delta T_y L_z}{P}. \quad (3)$$

The temperature differences $\Delta T_x = T_3 - T_1 > 0$ and $\Delta T_y = T_2 - T_1$ are related to temperatures probed by thermometers T3 and T1 and thermometers T2 and T1 for the longitudinal and transverse directions, respectively. Note that equations (2) and (3) also assume that the spatial separation ΔL_y between thermometers T2 and T1 is identical to the sample width L_y .

The experimental determination of the longitudinal and transverse thermal conductivities is thus accomplished by precise measurements of three temperatures T_1 , T_2 and T_3 , knowing the longitudinal and transversal distance of the thermometers ΔL_x and ΔL_y , the sample thickness L_z and measuring the heater power P .

3. Material and methods

The key components of our setup for highly sensitive THE measurements comprise: (1) a superconducting-coil cryomagnet providing stable magnetic fields and hosting the low-temperature sample space, and (2) a precise temperature control system based on field-independent thermometry with sub-mK accuracy. The latter is achieved by minimizing parasitic heat flows via the implementation of large thermal resistances, good thermal anchoring of cables and minimization of temperature gradients within the sample space. We build on the basic ideas

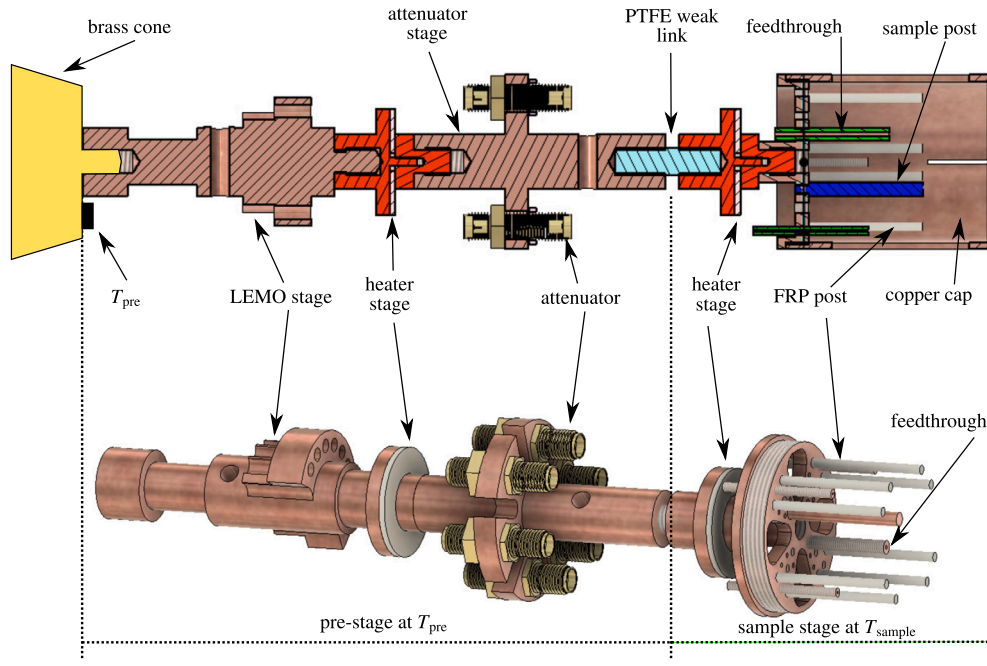


Fig. 1. (Top) Cross-section of the experimental stage based on modular components. The pre-stage and the sample stage are connected by a PTFE weak link. They are kept at the individually controlled temperatures T_{pre} and T_{sample} (thermometer location shown in Fig. 2), respectively. (Bottom) Rendered sample holder. Copper cap is not shown.

by Kim et al. [26] and adapt our modular design to improve performance in terms of functionality, measurement stability, space requirements and reproducibility. In the following we describe our system in detail.

3.1. Vertical cryomagnet

For the THE experiments we use a helium bath cryostat (AS Scientific Products Ltd.) with vertical magnet (VM) and a continuous flow variable temperature insert (VTI) shown in Fig. A.1. It provides the base environment for THE experiments with a surrounding gas temperature T_{VM} ranging from 1.5 K to 300 K and moderate magnetic field B up to ± 5 T along the vertical axis. Details are given in Appendix A.1.

It is worth noting that relying solely on temperature control through T_{VM} proved inadequate for achieving high temperature stability in both the sample temperature, T_{sample} , and the backend temperature of the sample holder, denoted as T_{pre} . This limitation arises due to the distances of about 100 mm and 30 mm between T_{VM} and T_{sample} , as well as T_{pre} , respectively (see Fig. A.1). In particular, we find that T_{pre} depends on the controlled T_{VM} , and, ultimately, on the He gas flow, that defines the cooling power. Note that controlling the needle valve for the He flow by He pressure or keeping its position fixed is not sufficient to maintain a stable long-term temperature, as the He cooling power changed with the level of liquid helium during measurements.

In order to achieve long-term temperature stability at the sample stage, it was necessary to apply a multi-stage thermalization approach to control the temperatures T_{VM} , T_{pre} and T_{sample} with $T_{VM} < T_{pre} < T_{sample}$ by use of independent proportional-integral controllers. The temperature difference $T_{pre} - T_{sample}$ defines the cooling power for the sample stage and the temperature gradients along the cables between the thermalization stages. To ensure stable temperature conditions and to simultaneously minimize temperature gradients in the cabling, it is important to maintain a reasonably high temperature difference between T_{pre} and T_{sample} , while also keeping it as low as possible. Typical mean values for sample heater power and temperatures probed at different locations on the experimental stage are summarized in Table A.1.

3.2. Experimental stage and sample stick

The VTI space of the VM accommodates a standalone sample stick which can be removed and independently handled for experiment preparation. This sample stick consists of a stainless steel tube and at its top is equipped with standard KF ports for evacuation, pressure gauging and electrical feed-through, including a 24-pin Fischer connector and eight grounded BNC connectors. The bottom part of the sample stick consists of a brass cone that connects to our custom-built experimental stage. The brass cone is encased by an aluminum cap that serves as vacuum enclosure and heat shield (Fig. 1 and Fig. A.1). Vacuum-tight sealing of the brass cone towards the sample stick is achieved using indium, while a vacuum-tight seal towards the sample stick is established with Apiezon N grease.

The modular experimental stage is mounted on the brass cone and consists of the pre-stage and the sample stage separated by a thermal weak link, realized by a 30 mm long M6 threaded rod made of polytetrafluoroethylene (PTFE). The pre-stage consists of the LEMO stage, the heater stage and the attenuator stage, all made from electrolytic tough-pitch (ETP) copper. The LEMO stage can hold up to eight PEEK-insulated four-terminal miniature LEMO connectors and has some notched space to wind wires around for their thermalization.

The heater stage hosts a flat tungsten metal ceramic heater (Thorlabs GmbH, HT19R). Magnetic leads of the as-delivered ceramic heater were removed and replaced by copper wires. The heater is pressed between two copper parts (red marked in Fig. 1) with moderate force, since higher contact pressures lead to an electrical short circuit. This heater and a calibrated Cernox thermometer (LS-CX-1050-BR-HT, Lake Shore Cryotronics Inc.) which is mounted on the brass cone are part of a control loop to regulate temperature T_{pre} .

Sensitive capacitance measurements require coaxial wiring, where the inner conductor poses a challenge for thermalization due to the low thermal conductivity of the shield. One key feature for the implementation of a thermal anchoring mechanism in our setup is the deployment of six 0 dB attenuators (XMA - Oni Spectra®, 4880-5523-00-CRYO) in the attenuator stage [29,30]. Compared to Kim et al.'s setup [26], our solution requires less space and works without tight winding of unshielded signal paths. The attenuator stage has equally spaced notches

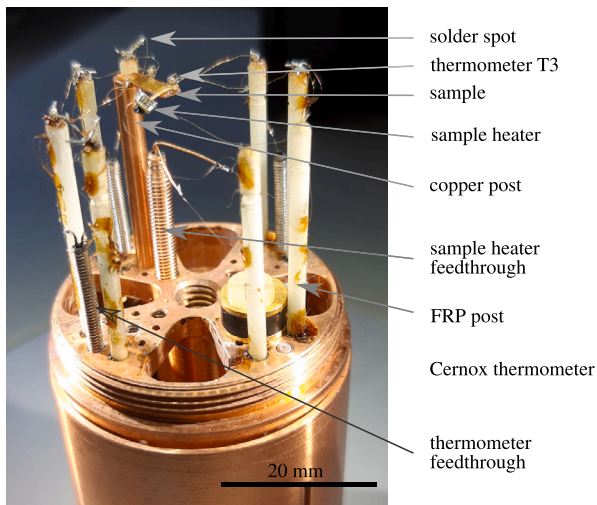


Fig. 2. Sample stage with copper and FRP posts serving as structural support. The sample is mounted on the copper post and is connected to a heater and three thermometers. Four custom-built copper feed-throughs serve as thermalization of electrical connections.

located between the attenuators in order to minimize eddy currents and possible heating induced by magnetic field ramping.

The sample stage consists of the same heater arrangement as installed at the pre-stage, a base plate and a threaded copper cap to reduce thermal radiation. A copper post, eight fiber-reinforced plastic (FRP) posts, a Cernox temperature sensor (CX-1030-CU-1.4L) measuring T_{sample} and four wire feed-throughs providing thermalization are arranged on the base plate. This base plate is perforated to reduce both, eddy currents and thermal mass (Fig. 2). The copper post serves simultaneously as sample holder and heat sink with temperature T_{sample} .

FRP posts are used to physically support wires of low thermal conductivity from the feed-throughs (40 mm \times \varnothing 25 μm manganin wire) and towards the thermometers (50 mm \times \varnothing 25 μm phosphor bronze wire). It is worth noting that the excess wire was looped up and down on the FRP posts, to further increase the effective thermal resistance. On top of each of these posts, a short silver-coated copper wire fixed with GE varnish is used as a solder spot to attach the micro-meter sized wires from the feed-throughs and the thermometers (Fig. 2).

We have also tried to use stacks made from Kapton and gold foils to provide the electrical contacts as proposed by Kim et al. [26]. However, we found that the thermal resistance of wires connected in series outperforms that of the stack solution. Furthermore, our solution employed a solder-based approach, which yields more reliable connections compared to a glue-based approach.

Thermal anchoring of the wires at the sample stage was essential to reduce parasitic heat flows. Therefore, custom-built wire feed-throughs were made of copper tubes and copper erosion electrodes that host insulated copper wires embedded in low-temperature adhesive (Stycast 2850 FT). The feed-throughs provide gold-plated miniature connectors on their back side (not visible in Fig. 2) which allowed for modular testing of electrical components.

3.3. Thermometry

The precise measurement of transverse and longitudinal thermal conductivities κ_{xx} and κ_{yy} relies on the temperature differences probed by thermometers T1, T2 and T3 (Fig. 3). These thermometers are required to provide high sensitivity and sufficient long-time stability in our targeted sample temperature range from 5 K to 100 K. Capacitive SrTiO₃ (STO) thermometers satisfy these demanding requirements and are highly suitable for THE measurements because of their relatively large permittivity variation and thus large capacitance variation with

temperature [25,26]. In order to keep control of their quality, our thermometers were manufactured by us following the procedure detailed below.

3.3.1. Thermometer fabrication

A commercial single crystal STO substrate (Crystal GmbH) of 15 mm \times 15 mm \times 0.5 mm size and (100) orientation was thinned and polished to a thickness of 100 μm . Both sides of the substrate were sputter-coated with an about 100 nm thick gold film. Afterwards, the gold-coated substrate was cut into pieces of 1 mm \times 1 mm and 1.5 mm \times 1.5 mm, discarding its edge pieces to avoid electrical short circuits through the gold coating on the substrate's edges. Only thermometers with an edge length of 1.5 mm are used for the measurements carried out in this study.

Both sides of the gold-plated STO thermometers are connected with 50 mm long and 25 μm thick insulated phosphor bronze wires (Goodfellow GmbH, CU055810). For low-impedance electrical connections, the polyimide wire insulation was removed by mechanical scratching and tin-coating at about 450 $^{\circ}\text{C}$ using solder flux (solder oil "ST", Felder GMBH Löttechnik). Before integration, the prepared wires were test-soldered and checked for electric current transmission.

In order to mechanically and electrically attach the prepared phosphor bronze wire on one side of the gold-plated face of the STO thermometer a small droplet of silver epoxy (EJ2189-LV, EPO-TEK[®]) was used (inset in Fig. 3). This connection was annealed at 300 $^{\circ}\text{C}$ for 2 min. The same procedure was used to connect the other gold-plated face. Finally, the room temperature capacitance of the thermometers was checked to be about 50 pF.

3.3.2. Sample and thermometer assembly

For demonstration of the instrument performance, we have chosen the pyrochlore oxide terbium titanate Tb₂Ti₂O₇ as reference material. Tb₂Ti₂O₇ shows a moderate transverse thermal conductivity $\kappa_{yy} = 1.2 \times 10^{-3} \text{ W K}^{-1} \text{ m}^{-1}$ at $B = 8 \text{ T}$ and $T = 12.8 \text{ K}$ and a pronounced Hall angle κ_{xy}/κ_{xx} with a maximum value of 0.44 % giving rise to a significant transverse temperature gradient for millimeter-sized samples and magnetic fields in the range of a few Tesla [1]. Our used high-quality Tb₂Ti₂O₇ crystal [31] was grown by the Czochralski method at the Leibniz-Institut für Kristallzüchtung (Berlin, Germany). The sample was annealed at 500 $^{\circ}\text{C}$ for 12 h in air after previously performed laser flash measurements described elsewhere [31], resulting in a change in the crystal's color, apparently becoming slightly brighter/yellower during this entire procedure.

Using X-ray Laue diffraction, the sample surface was oriented, polished and cut, with the surface normal of the largest face being parallel to the magnetic easy axis along the [111] direction [32] and the longitudinal heat transport along the sample length along [1 $\bar{1}$ 0], to allow for direct comparison with previous works. The sample size was 8.22 mm \times 2.31 mm \times 0.327 mm.

To reach negligible influence of thermal connections and to reach short thermal equilibration times, the as-prepared thermometers were directly glued to the sample (Fig. 3), thus ensuring a low thermal mass. Small amounts of GE varnish diluted with ethanol were placed on the desired position and the thermometers were pressed onto the side faces of the sample, so that the [100] direction of the STO thermometers was parallel to the direction of the heat flow. This positioning of the thermometers leaves only a small contact surface and thus low mechanical stability. Therefore small, almost dried GE varnish pellets were placed between the thermometers and sample as mechanical support (Fig. 3). Finally, for each thermometer, the GE was cured for 2 min at 200 $^{\circ}\text{C}$. Since the warm GE is quite soft, the end position of the thermometers were corrected during cool-down.

3.3.3. Electronic circuitry and readout devices

Capacitance measurements at low temperatures require coaxial cables with low thermal conductivity. Here, ultra-miniature coaxial cables

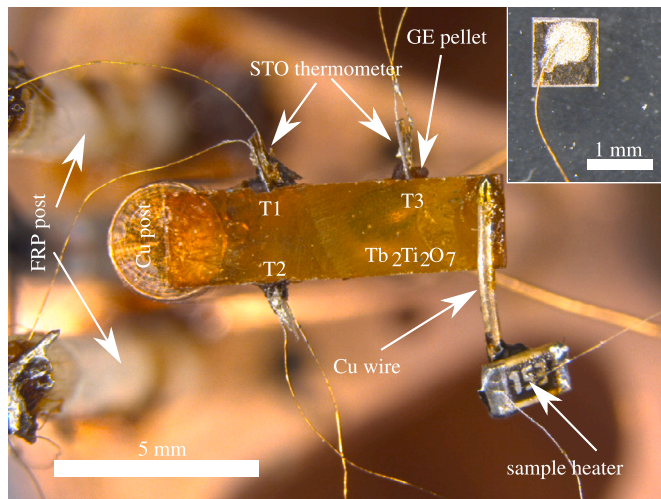


Fig. 3. $\text{Tb}_2\text{Ti}_2\text{O}_7$ sample glued to the copper heat sink. Thermometers are directly attached to the sample. The resistive sample heater is attached via silver-coated copper wire. The inset shows the top view of a thermometer with one phosphor bronze wire attached.

with stranded 304 stainless steel conductors (Lakeshore type SS) were used to connect the coaxial feed-throughs with the 0 dB attenuators. In order to reduce ground loops, the shielding potential was only connected at the attenuator stage. The same coaxial cables were used to connect the attenuators with the self-built wire feed-throughs at the experimental stage, also with their shields connected at the attenuator side acting as the center in a star ground layout.

The connections between the 24-pin Fischer connectors and the 4-pin LEMO connectors were realized by 12-pair $\varnothing 110 \mu\text{m}$ constantan ribbon cables (CMR-CWL-12CO-5m, CMR-Direct). The Cernox thermometer packages were connected in four-point configuration with the 4-pin LEMO connectors by Quad-Lead™ cryogenic phosphor bronze wire. The LEMO connector for the sample heater and the 4-pin self-built wire feed-through were connected by four single cores of the constantan ribbon cable. Four channels of the 24-pin Fischer connector connect the ceramic heaters in two-point configuration using $\varnothing 0.22 \text{ mm}$ insulated copper wire. Copper wires were used to avoid resistive heating of the wires while powering the 30Ω ceramic heaters. Table A.2 lists the pin assignment of heaters and temperature sensors and the cable materials used. Outside the cryostat, shielded coaxial and shielded Belden 8728 CM cables were routed far away from stray magnetic fields to avoid any interference.

The capacitance of thermometer T3 was measured by an AH 2500A (Andeen-Hagerling INC.) capacitance bridge operated with fixed frequency $f_3 = 1000 \text{ Hz}$. For thermometers T1 and T2, the capacitances were measured using two independent AH 2700A Option-E capacitance bridges (Andeen-Hagerling INC.) at frequencies of $f_1 = 1200 \text{ Hz}$ and $f_2 = 1400 \text{ Hz}$, respectively. These frequencies were chosen because they are the nearest discrete settings to the 1000 Hz setting, which provides the best instrumental resolution. Due to the application of different frequencies, all bridges can be operated simultaneously and without the need of switching units limiting the time for data acquisition. In situations where switching remains unavoidable, we recommend thermalization of the switching devices, as our available units (Keithley 7709) showed an internal capacitance that was highly susceptible to variations of the environment temperature.

For temperature readout and control, three LakeShore temperature controllers (two models LS340 and one model LS350) were used. These controllers allow for multi-channel temperature monitoring and temperature control with individual PID values. The assignment of thermometer sensors and control loops is summarized in Table A.3.

For ultra-low noise current control of the sample heater, a precision current source (CS580, Stanford Research Systems) was used and

controlled by an optical interface controller (SX199, Stanford Research Systems). The voltage drop at the heater was measured with a data acquisition logging multimeter system (DAQ6510, Keithley).

It is important to note that the measurement devices, especially the temperature controllers, were kept in a temperature-controlled environment. Here, we used a thermally isolated rack with fan control to hold the inner temperature at $(300.00 \pm 0.02) \text{ K}$. Under non-stabilized conditions, temperatures measured by STO thermometers were influenced by room temperature variations. These variations were caused by the room temperature dependent readout (0.001% of the reading/ $^\circ\text{C}$) of the temperature controller and its adjustment of the heating power, which was consistent with the controller's specification.

4. Results and discussion

4.1. Measurement description

During the experiment three distinct measurement sequences were performed: temperature calibrations, power calibrations (longitudinal thermal conductivity measurements), and B field sweeps. For each of these measurement protocols, the thermometer capacitances are collected in thermal equilibrium. In the temperature calibration mode, T_{sample} was stabilized at zero sample heater power and zero B field. Power calibrations were performed by incrementally increasing the sample heater power at zero B field. B field sweeps were conducted for stabilized sample temperature with a fixed sample heater power. The measurement modes are shown in Fig. A.2.

Since the extraction of the transverse temperature necessitates anti-symmetrization, data is acquired for both B orientations with equal absolute value. We utilized two distinct sweep sequences: 1) linear steps with decreasing field between maximum (positive) and minimum (negative) magnetic field, with step widths of either 0.5 T or 1 T and 2) sawtooth-like sweeps, switching the B field direction for a chosen set of discrete B values combined with zero-field measurements (e.g. $B = [0, 5, 0, -5, 0, 4, 0, -4, 0, \dots, 0, 1, -1, 0] \text{ T}$). Fig. A.3 illustrates the two different types of sweeps.

The linear step approach assumes fluctuation free conditions over the entire scan. In order to accurately correct for slight drifts in the thermometers' capacitance values over time, it was necessary to acquire a sufficient number of data points at $B = 0$ before and after the sweep. The sawtooth-like sweeps approach offers the advantage of addressing non-linear baseline behavior and rapid baseline fluctuations. However, this advantage comes at the cost of an extended measurement time.

Fig. A.3 shows the baseline change of T1 and T2 in zero-field to be linear and fluctuation free over a time span of three days with 1.15 mK d^{-1} and 1.73 mK d^{-1} , respectively. The stability and linearity of the drift behavior facilitate the execution of linear step sweeps. In our setup, both sweep approaches give comparable results (Figs. 7, 8a).

A proper thermal anchoring of the sample stage is essential for maintaining the above mentioned drift behavior, which is especially important to keep during helium fillings. Fig. A.3 clearly demonstrates the successful functioning of our thermal anchoring method. While during filling the temperature of the variable temperature insert T_{VM} changes by several Kelvin, the temperature of the sample shows a five-day standard deviation of $110 \mu\text{K}$. The capacitance values of the thermometers are independent of the temperatures of previous stages, which is essential for the THE setup to work accurately.

4.2. Temperature calibration

Our capacitance thermometers can be modeled as parallel capacitor plates whose temperature dependent capacitance depends on the dielectric constant $\epsilon_r(T)$. Previous models have been proposed to describe the $\epsilon_r(T)$ of STO by a modified Curie-Weiss model [33] or Barrett's formula [34]. As using these models results in moderate deviations,

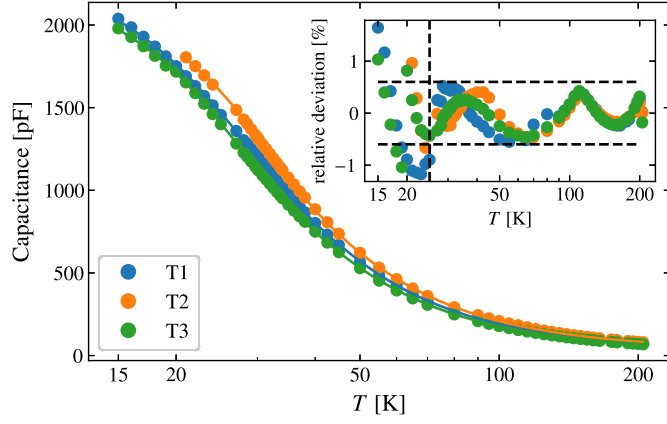


Fig. 4. Capacitance of the thermometers as a function of temperature for the T_{CAL} set. Data of three thermometers is fitted using the sum of a rational function and a third-order polynomial (Eq. (4)). The inset shows the relative deviation of the thermometer calibration.

our strategy involved enhancing the degree of freedom through modifications to the mentioned models and incorporating known models characterizing cryogenic material properties [35] leading to a set of 21 comprehensive fitting models, as outlined in Table A.4. Using these functions we considered to fit capacitance $C(T)$ as well as temperature $T(C)$. This two-fold strategy is driven by the physical motivation behind fitting $C(T)$ and the computational efficiency of applying a $T(C)$ fit for temperature evaluations.

In order to compare various interpretations of temperature equilibrium, we selected five different temperature-capacitance sets using the temporal derivatives of the sample holder temperature and capacitances with different threshold values as filter criteria (Table A.5). One of these sets only contains data from the previous mentioned temperature calibration and power calibrations for $P = 0$, referred to as T_{CAL} set within the paper.

Among these 210 potential fits, we selected thirteen fits based on their lowest absolute and relative deviations for all three thermometers (Table A.6). These different selections of calibration data points and fit models are used to demonstrate the effect of individual decisions for the follow-up data analysis.

We find that the sum of a rational function and a third-order polynomial fitting (*rational poly 3* in Table A.4) consistently results in minimal absolute and relative deviations for the $T(C)$ fits across various selections of calibration data points (Fig. A.4). In specific cases a logarithmic polynomial of sixth order (*log poly 6*) shows lower deviation. The fit of $C(T)$ works well with a third-order rational function (*rational function*) and the logarithmic polynomial of sixth order. For more details consider Appendix A.4.

Fig. 4 shows the capacitance of the thermometers of the T_{CAL} set as a function of temperature. As expected, a strong increase in capacitance for decreasing temperatures is observed. This data set shows best fit results for the sum of a rational function and a third-order polynomial fitting given by

$$T(C) = \frac{A_1 A_3 - A_2 - A_3 C}{A_1 - C} + A_4 C + A_5 C^2 + A_6 C^3 \quad (4)$$

with C the measured capacitance and A_i the fitting parameters. This model was inspired by the modified Curie-Weiss function with constants substituted by polynomials up to third order. The inset of Fig. 4 shows that the thermometers are well calibrated with a maximum relative deviation less than 0.6% in our relevant measurement range from 25 K to 200 K. We adopt this calibration method for analysis shown in the main text. We also explore the impact of choosing alternative configurations in the Appendix. Unfortunately, our setup failed to measure the capacitance of T2 between 1500 pF and 1600 pF and beyond 1800 pF in a reversible manner.

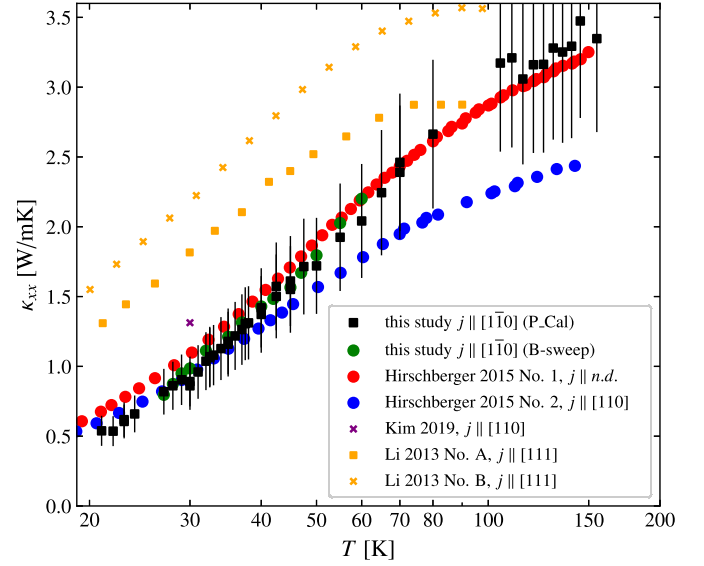


Fig. 5. Longitudinal thermal conductivity κ_{xx} compared to literature [1,26,32]. The black data points show the results from the analysis of our thermal conductivity measurements, taking into account the slopes $\partial T_{[1,2,3]}/\partial P$. Error bars indicate an 20% error. The green points represent results from the analysis of our B -sweeps taking absolute temperature differences into account.

4.3. Longitudinal thermal conductivity $\kappa_{xx}(T, B)$

Applying the previously mentioned thermometer calibration, Fig. 5 presents a comparison of our results for the zero-field longitudinal thermal conductivity $\kappa_{xx}(B = 0)$ in single crystalline $Tb_2Ti_2O_7$ with literature data [1,26,32]. The overall behavior of $\kappa_{xx}(B = 0)$ is consistent with previous results, indicating low thermal conductivity and the lack of a low- T maximum, commonly observed in conventional phonon dominated systems. This phonon-glass-like behavior originates from strong spin fluctuations in the spin-liquid state causing strong phonon scattering, present to even higher temperatures [32].

Generally, the zero field thermal conductivity tensor of $Tb_2Ti_2O_7$ is expected to be isotropic due to its cubic crystal structure. However, literature reports significant sample-to-sample deviations [32], even in cases with identical orientations as shown in Fig. 5. These deviations might be explained by different levels of defect concentrations or systematic measurement uncertainties. Estimating a systematic error of 20% mainly introduced by uncertainties in the sample geometry, Hirschberger et al. [36] could not resolve a possible anisotropy in κ_{xx} within his data set. With respect to this uncertainty, our data is comparable with Kim et al.'s results and in agreement with Hirschberger et al.'s results. Interestingly, our κ_{xx} data matches that of Hirschberger et al.'s sample 1 for $T > 42$ K, albeit the direction of heat flow was not aligned with one of the crystallographic axes in their experiment. For $T < 42$ K, we observe excellent agreement with their sample 2, which has an identical heat flow direction along [110].

Fig. 5 shows a comparison of $\kappa_{xx}(B = 0)$ for different analysis methods. The black points show the calculated $\kappa_{xx}(B = 0)$, by analyzing the power calibration data for which the slopes of $\partial T_{[1,2,3]}/\partial P$ are used to obtain

$$\kappa_{xx}(B = 0) = \left(\frac{\partial T_3}{\partial P} - \frac{1}{2} \left(\frac{\partial T_1}{\partial P} + \frac{\partial T_2}{\partial P} \right) \right)^{-1} \frac{L_x}{L_y L_z}. \quad (5)$$

This method proves to be robust against temperature offsets and the choice of the calibration, as indicated by the small error bars shown in Fig. A.8.

As usually done for continuous T -sweeps at fixed P and B and as likely performed in previous work, we also extracted κ_{xx} from B -sweep data using the applied fixed sample heater power P and the absolute

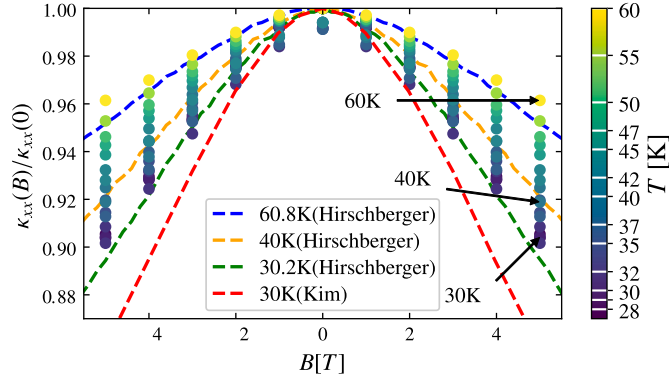


Fig. 6. Relative longitudinal thermal conductivity κ_{xx} as function of B compared with literature values [1,26].

longitudinal temperature differences. While this method is in agreement with the previous method (Fig. 5) for the chosen thermometer calibration, we find that alternative thermometer calibration choices can have a significant effect on κ_{xx} (Fig. A.8). This difference arises because offset compensation is not integrated into this approach. Deviations up to 50% are observed for our selected set of thermometer calibrations. It is evident that the absolute temperature differences are subject to offsets and generate the striking differences in κ_{xx} between different calibrations, which may partially account for the previously observed sample-to-sample deviations.

Obviously, these deviations also appear in $\kappa_{xx}(B, T)$ (Fig. A.9 a, b), which have a significant impact on the results for the transverse thermal conductivity $\kappa_{xy}(B, T)$, since $\kappa_{xx}(B, T)$ enters quadratically into the calculation. In contrast, we find that the deviation for the relative change $\kappa_{xx}(B, T)/\kappa_{xx}(0, T)$ only is in the order of about 3% for the set of thermometer calibrations (Fig. A.9 c, d). To minimize the uncertainties introduced by thermometer calibration in $\kappa_{xx}(B, T)$, we therefore propose utilizing the relative change $\kappa_{xx}(B, T)/\kappa_{xx}(0, T)$ with respect to $\kappa_{xx}(0, T)$, as robustly determined by Eq. (5). The field-dependent longitudinal thermal conductivity $\kappa_{xx}(B, T)$ is shown in Fig. A.10. In agreement with previous reports [1,26], we observe decreasing κ_{xx} with increasing B .

In order to compare the strength of the relative magneto-thermal conductivity, $\kappa_{xx}(B)/\kappa_{xx}(0)$ is analyzed as shown in Fig. 6. Taking into account the about 3% uncertainty at $B = 5$ T coming from the thermometer calibration, our data points show good agreement with data from Hirschberger's sample 1 (as represented by the dashed lines in Fig. 6). As shown in Fig. A.9, other thermometer calibrations provide even better agreement for 30 K, but slightly higher deviation for 40 K. In contrast, larger deviations from the data set published by Kim et al. are observed, which cannot be explained by our selection of thermometer calibrations.

4.4. Transverse temperature difference ΔT_y

The transverse temperature difference ΔT_y at fixed P is obtained by anti-symmetrization

$$\Delta T_y(B) = \frac{1}{2} \left((T_2(B) - T_2(-B)) - (T_1(B) - T_1(-B)) \right), \quad (6)$$

where T_1 and T_2 are the averaged temperatures for the given B fields. The anti-symmetrization is an important step to remove any symmetric signals, such as the thermometers field dependence (Fig. A.7). Our field dependence measured at 30 K is about four times higher than previously reported values at 4.2 K [25]. The observed field dependence is likely a result of technical factors, such as shifting leads, rather than being an intrinsic property of the material.

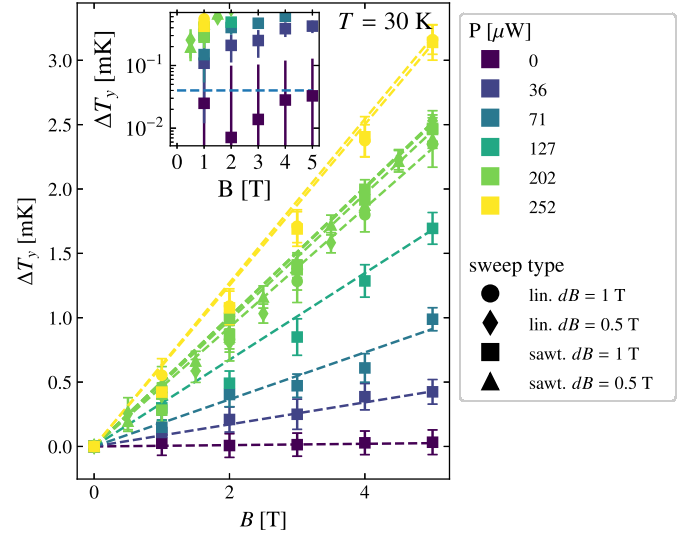


Fig. 7. The transverse temperature difference ΔT_y as function of B for a set of sample heating powers and a sample temperature of 30 K. Dashed lines show linear fits for individual B -sweeps. The inset shows a magnification with logarithmic scale with an estimated maximum noise level of about 40 μ K indicated by the dashed line.

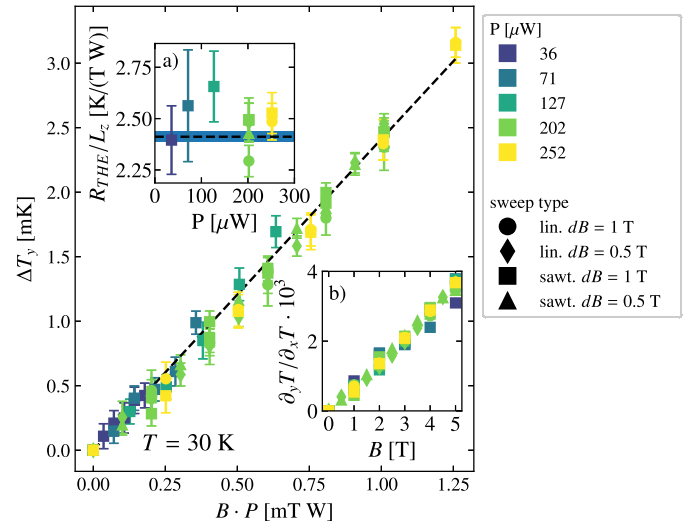


Fig. 8. Linear dependence of ΔT_y on the product $B \cdot P$, here shown for a sample temperature of 30 K. The experiment at 202 μ W power was performed in four different configurations, sawtooth repeated twice. The experiment at 252 μ W was performed in both, the linear and sawtooth configuration. The dashed line shows the linear fit using all data points. a) The inset shows the slope of individual B -sweeps. The dashed line in the inset indicates the slope obtained by taking into account all data points. The corresponding standard deviation is indicated by the area marked blue. b) The inset shows the Hall angle ratio at a sample temperature of 30 K.

We calculate the uncertainty by

$$err(\Delta T_y) = \frac{1}{2} \sqrt{\Delta T_1^2(B) + \Delta T_1^2(-B) + \Delta T_2^2(B) + \Delta T_2^2(-B)}, \quad (7)$$

where ΔT_1 and ΔT_2 are the standard deviations of the temperatures measured in equilibrium. An overview of measured $\Delta T_y(B)$ for different sample temperatures, powers, sweep types and temperature calibrations is given in Fig. A.11.

Fig. 7 shows the transverse temperature difference for different powers and B -sweep types at 30 K. As expected, ΔT_y depends linearly on B and increases with increasing heating power. Our setup clearly resolves temperature differences as small as 100 μ K at 30 K, as is demonstrated

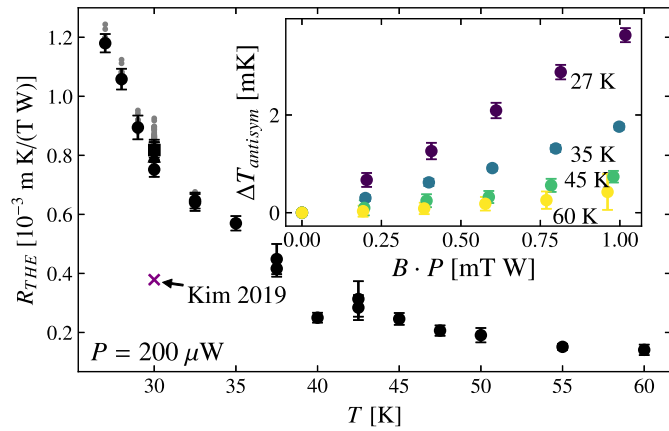


Fig. 9. Thermal Hall constant R_{THE} is shown as function of temperature for $P = 200 \mu\text{W}$. The green cross represents literature data [26]. Gray points represent results for different choices of thermometer calibrations (Table A.6). The inset shows a selection of transverse temperature differences at different sample temperatures.

by the data collected at lowest power $P = 36 \mu\text{W}$. For zero power, no significant change of ΔT_y is observed and the maximum signal of $40 \mu\text{K}$ is within the noise level of the setup, as shown in the inset of Fig. 7. A further discussion of our instrument resolution is deferred to section 4.7.

4.5. The thermal Hall constant R_{THE}

For the conventional Hall effect, the transverse potential is proportional to $B \cdot I$, with I the electronic current and the proportionality constant being related to the charge carrier density. In analogy, for low B -fields, we expect the transverse temperature gradient ΔT_y to be proportional to $B \cdot \dot{Q} \propto B \cdot P$, with \dot{Q} the amount of heat transferred per unit time. As shown in Fig. 8, this behavior is valid for different powers and B -sweep types, which provides a strong argument that the measured signals are intrinsic to the THE. The analysis of the slope of individual powers is summarized in the inset (a) of Fig. 8. This demonstrates that taking into account all data acquired with different powers yields a much lower fitting error (light blue bar in the inset of Fig. 8) than the individual analysis. In analogy to the conventional Hall effect we define the thermal Hall constant to be

$$R_{\text{THE}} = L_z \frac{\partial \Delta T_y}{\partial (B \cdot P)}. \quad (8)$$

The temperature-dependent thermal Hall constant is shown in Fig. 9. For comparison, we extracted data from Kim [26] to calculate R_{THE} for identical heating power and found it to be about half of our values. We can exclude different thermometer calibrations to cause this deviation, which is indicated by the gray points in Fig. 9. As both samples have identical orientation we have to conclude that this difference is intrinsic to the samples or stems from other systematic issues.

4.6. Thermal Hall conductivity $\kappa_{xy}(T)$

To compare the temperature dependent κ_{xy} with the literature we analyze the entropy and field independent quantity

$$\left[\kappa_{xy} / (B \cdot T) \right]_0 = \lim_{B \rightarrow 0} \kappa_{xy} / (B \cdot T). \quad (9)$$

To numerically evaluate the zero-field limit, a polynomial fit was used by Hirschberger et al. [36]. To ensure consistency in the data analysis, we digitized from Hirschberger et al.'s data [36] and found the best agreement with the published data for a fourth-order polynomial. This is a reasonable choice, since $\kappa_{xx}(B)$ can be approximated by a quadratic function. We applied the same analysis procedure to digi-

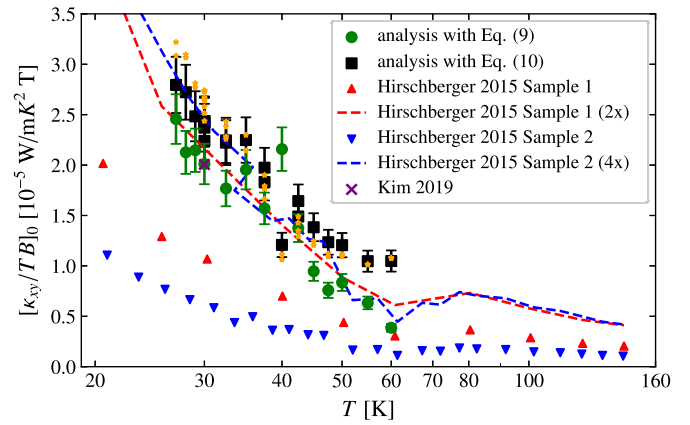


Fig. 10. Reduced transverse thermal conductivity compared with literature data [1,26]. Orange points are results for different choices of thermometer calibrations.

tized raw data taken from the publication by Kim et al. [26] and to our data (see Fig. A.12).

Our results, shown in Fig. 10, are in excellent agreement with Kim et al.'s data [26] for the transverse thermal conductivity at 30 K, despite our differing R_{THE} values. This is attributed to the fact that Kim et al. obtained a higher value for κ_{xx} , which compensates the lower value of R_{THE} in their calculation of κ_{xy} .

Despite the significant difference in absolute values with respect to those of Hirschberger et al., we find that scaling their thermal conductivity values by a constant factor results in a temperature dependence that is consistent with our findings as shown by the dashed lines in Fig. 10 when applying a constant scaling factor of 2 and 4 for samples 1 and 2, respectively. We presume, that the observed differences for the absolute values are most likely due to systematic errors and calibration offsets introduced by the uncertainty in κ_{xx} .

As discussed above, the calculation of κ_{xy} can lead to significant variations depending on the analysis method for the determination of κ_{xx} . In order to keep uncertainties low, we used $\kappa_{xx}(B=0)$ obtained from Eq. (5) and applied the relative changes in order to get $\kappa_{xx}(B)$ as previously proposed (Fig. A.10). Error bars in Fig. 10 include the uncertainty of $\kappa_{xx}(B=0)$ and the uncertainty of $\kappa_{xx}(B)/\kappa_{xx}(B=0)$ due to the thermometer calibration.

It is possible to also employ an alternative analysis method, using the longitudinal thermal conductivity obtained from Eq. (5) and the thermal Hall constant using the following relation

$$\left[\kappa_{xy} / (B \cdot T) \right]_0 \approx \frac{1}{T} \left[\kappa_{xx}(B=0) \right]^2 \cdot R_{\text{THE}}. \quad (10)$$

Our detailed analysis, which allows for a set of thermometer calibrations, reveals that the precise thermometer calibration is crucial. Small variations in thermometer calibration result in significant variations of $[\kappa_{xy} / (B \cdot T)]_0$. This is indicated by the orange points in Fig. 10, which show the results calculated for different thermometer calibrations. Our results demonstrate, however, that the two alternative analyses, either based on Eq. (9) or on Eq. (10), yield comparable results.

4.7. Temperature resolution

Finally, we compare the performance of our setup in terms of temperature resolution with that of Kim et al. [26]. Our thermometer capacitance values are approximately seven times larger than those of Kim et al.'s thermometers, despite our surface area being increased by only a factor of 2.25. The reason for that might be a geometrical error or differences in the contact surfaces, so that surface charging might play a role. Nevertheless, the dimensionless sensitivity of our thermometers compares well with that reported by Kim et al.

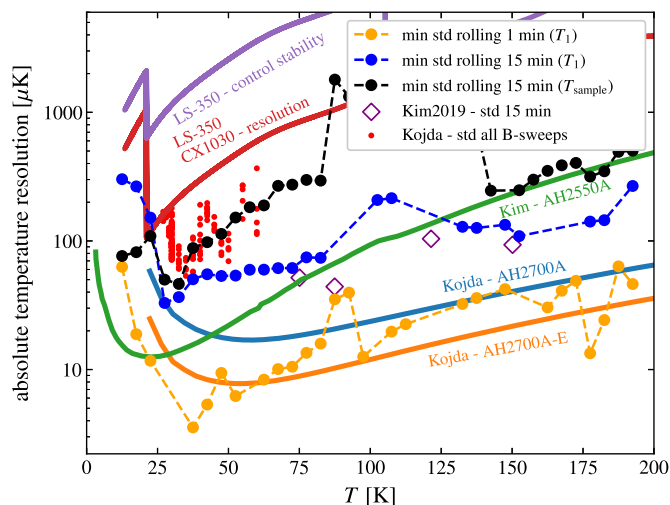


Fig. 11. The minimum standard deviation of temperature measurements taken for 1 min, 3 min, and 15 min data acquisition time, representing the minimum system noise (non-drift corrected) as a function of temperature (dashed lines). Purple diamonds show the standard deviation for 15 min long sequences of a reference system [26]. Red points show the standard deviation of thermometer T1 for all conducted B-sweeps. Calculated absolute temperature resolution of our setup (solid blue and orange) compared to a reference system (solid green) [26]. The solid red curve shows the temperature display resolution of the system that controls the sample holder temperature. The violet curve shows the specified control stability. The jumps are a result of the resistance measurement resolution, as specified.

We determine the absolute temperature resolution ϵ_T of our system in analogy to Kim et al.'s procedure using the equation:

$$\epsilon_T = \frac{\epsilon_C(C(T))}{\partial C / \partial T}. \quad (11)$$

Here, $\epsilon_C(C(T))$ is the temperature-dependent resolution of the measurement system, which is calculated from the manufacturer's specification. This calculation includes the capacitance bridge settings, such as excitation voltage, frequency and integration time as well as the measured capacitance and loss values of our thermometers.

As shown in Fig. 11, our thermometers demonstrate a minimum temperature resolution of 7.5 μK at 50 K, which is significantly better than the performance of Kim et al.'s thermometers, which achieve a minimum resolution of 12.5 μK at 22.5 K. For temperatures above 29.5 K, our setup outperforms that by Kim et al. due to higher $\partial C / \partial T$ and the use of measurement devices with higher resolution. In particular, we show the performance improvement obtained by using option E of the AH2700A capacitance bridge, which provides higher precision (albeit at a higher cost) and achieves a resolution below 30 μK over the entire temperature range shown. As shown in Fig. 11, the minimum resolution increases for $T < 40$ K. This is due to the increasing $C(T)$ leading to increasing ϵ_T and a reduced ability to accurately capacitance changes. To maintain high resolution at low temperatures it might be helpful to reduce the absolute capacitance by geometry optimization and optimize $\partial C / \partial T$ by modification of the permittivity using doping [37].

To identify potential resolution limitations, we compare the absolute temperature resolution with the system noise, which is given by the standard deviation for a given integration time. We calculate the standard deviation for the entire non-drift-corrected data set and show the minimum value for a binning of 5 K width. As shown in Fig. 11, our 'one-minute' system noise (averaging over 5 measurements) compares well with the ideal temperature resolution. The 15 min standard deviation for our system shows slightly higher values than the reference system, which may be due to our analysis of non-drift-corrected values. As previously mentioned, our thermometers exhibit a drift of

1.15 mK d^{-1} , which corresponds to a drift of 12 μK during a 15 min time span.

We investigated the standard deviations of thermometer T1 for B-sweeps with $B > 0$ taken for time intervals ≤ 15 min after drift correction (red points in Fig. 11). All values were found to be equal to or higher than the minimum rolling 15 min standard deviation. However, the distribution of values exhibits a rather large spread, with maximum deviations about four times higher than the minimum. To determine the origin of this noise, we analyzed the resolution and electronic control stability of our sample holder temperature control system using the LS350 and a Cernox CX1050 sensor. Fig. 11 shows that our noise level is well below the electronic control stability and mostly lower than the display resolution. Our sample holder is heavily decoupled (low cooling power) and temperature controllers are set to maximum integration times, which ensures that our noise level is well below the electronic control stability. However, the maximum system noise is reflected in the display resolution (red curve in Fig. 11), which we believe to be the most likely origin of the noise measured by our much more precise capacitance thermometers.

Further measurement stability suffers from a measurement range change of the temperature controller seen as spike in Fig. 11 around 25 K. Below this limit, both rolling standard deviations for T1 show significantly enhanced values providing experimental indication of worse control stability. The latter arguments imply a strongly enhanced temperature control mechanism for the sample holder.

5. Conclusion

The focus of our work was the development of an advanced setup for high-precision thermal Hall measurements that utilized ultra-sensitive capacitive thermometry. Our setup represents a significant improvement in terms of resolution, long-term stability, reproducibility and size of the thermal anchoring mechanism. It is worth noting that our setup underwent numerous internal iterations before achieving the final results presented here.

Throughout the course of our research, we faced significant experimental challenges, especially concerning thermal anchoring and long-term stability. We successfully addressed these issues and report our solutions, which have resulted in an extraordinary high temperature resolution. This accomplishment is attributed to a combination of high-precision thermometry, thermal anchoring, multi-stage experimental thermalization, and thermalized high-precision electronics.

We present the temperature resolution and system noise analysis of our setup with an ideal resolution of 7 μK . Our setup is capable to resolve temperature differences below 100 μK with a minimum background signal of 40 μK . We identify the sample holder stabilization as current limitation for higher precision showing temperature noise on the order of our resolution. This systematic noise is far below the specified control stability, which was achieved by use of a weak linked sample holder of adequate thermal mass and long PI integration times of the temperature controller.

Our results highlight the importance of careful analysis and optimization of all components in the experimental setup to achieve the highest precision and accuracy in temperature measurements. For next generation THE setups we recommend exploring advanced temperature stabilization methods for the sample holder, preferably employing a combination of Cernox and capacitance thermometers. In this approach, the Cernox thermometer can be employed for calibration purposes, while the control loop can be switched to maintain a constant capacitance whenever low noise performance is desired. This could give better long term stability and also excludes B field dependencies and B field induced control feedback during B sweeps.

We used our setup to investigate terbium titanate confirming the temperature-dependent longitudinal and transverse conductivity literature data. We show conclusively that the precise thermometer calibration plays a crucial role for the accuracy of THE data even if standard

analysis of the THE effect employs temperature differences which removes part of the systematic errors. We quantitatively investigate the robustness of thermal Hall effect data with respect to thermometer calibration, emphasizing the importance of accurate thermometer calibration for the conclusions drawn from THE data. In particular, we demonstrate significantly enhanced accuracy for the longitudinal thermal conductivity κ_{xx} and consequently for the transverse thermal conductivity κ_{xy} when relying on changes of the temperature with heating power rather than extracting κ_{xx} from magnetic field sweeps at fixed heater power and using absolute temperature differences. To further enhance precision, we base the analysis of the temperature differences on the product $B \cdot P$, rather than using the bare magnetic field dependence to extract temperature differences. This approach has proven to work excellent within the linear regime of the THE, which remained applicable for fields up to 5 T in our study.

In analogy to the conventional Hall effect, we introduce the thermal Hall constant R_{THE} in the field of thermal Hall effects and demonstrate how to obtain R_{THE} from experimental data. We demonstrate the precision and robustness of our $B \cdot P$ method when extracting the thermal Hall constant. Analyzing R_{THE} with highest resolution will pave the way to investigate quantization effects of the thermal Hall conductivity and allows for higher sensitivity for exotic particles or phase transitions in future THE experiments.

Finally, well-defined measurement and analysis protocols, in addition to the bare instrumental resolution, are crucial for comparative work in the field of THE measurements. The definition of a reliable THE reference material would be beneficial for validating and benchmarking existing and future instruments. Good metals like gold or silver, where the Righi-Leduc effect can be measured in thinned sheets, are potential candidates for such reference materials [38].

Appendix A

A.1. Details and technical drawing of the vertical magnet

For the THE experiments we use a helium bath cryo-magnet (AS Scientific Products Ltd.) with vertical magnetic-field geometry shown in Fig. A.1. This is a modified version of an orange standard cryostat with a continuous flow variable temperature insert (VTI) that provides a temperature range from 1.5 K to 300 K. It allows for a maximum sample stick diameter of 48 mm. The cryostat hosts a pair of superconducting Helmholtz coils to generate a symmetric vertical magnetic field up to 5 T with a deviation of less than 0.1 % in a region extending to 20 mm in height [39].

The VTI of the cryostat is thermally coupled to the evaporation chamber and acts as a link between the evaporation chamber and the sample stick. Heat conduction through the VTI occurs via the baffles and the presence of 20 mbar helium gas inside the VTI. Continuously pumping the evaporation chamber generates the necessary cooling power. In order to largely suppress any external energy intake by vibrations, the pump lines and evaporator lines are routed through two sand-filled boxes sized 1.2 m \times 0.8 m \times 0.2 m. Furthermore, the cryostat is placed on rubber mats providing additional vibrational decoupling.

The He flow and thus the cooling power are regulated by a motor-controlled cold needle valve. Its position is adjusted by a feedback loop to which the evaporation chamber pressure serves as input parameter. The gas temperature T_{VM} in the evaporation chamber is measured with a Cernox temperature sensor and is controlled by a resistive heater.

CRediT authorship contribution statement

Danny Kojda: Conceptualization, Data curation, Formal analysis, Investigation, Methodology, Project administration, Resources, Software, Validation, Visualization, Writing – original draft, Writing – review & editing. **Ida Sigusch:** Conceptualization, Methodology, Software. **Bastian Klemke:** Methodology, Resources, Software. **Sebastian Gerischer:** Methodology, Resources, Software. **Klaus Kiefer:** Methodology, Resources. **Katharina Fritsch:** Resources, Writing – review & editing. **Christo Gugushev:** Resources. **Klaus Habicht:** Conceptualization, Funding acquisition, Project administration, Supervision, Writing – original draft, Writing – review & editing.

Declaration of competing interest

The authors declare that they have no known competing financial interests or personal relationships that could have appeared to influence the work reported in this paper.

Data availability

Data will be made available on request.

Funding

This research did not receive any specific grant from funding agencies in the public, commercial, or not-for-profit sectors.

Acknowledgements

We highly acknowledge the technical support by J. E. Hoffmann, K. Quoll, C. Förster and A. Steigert (all HZB).

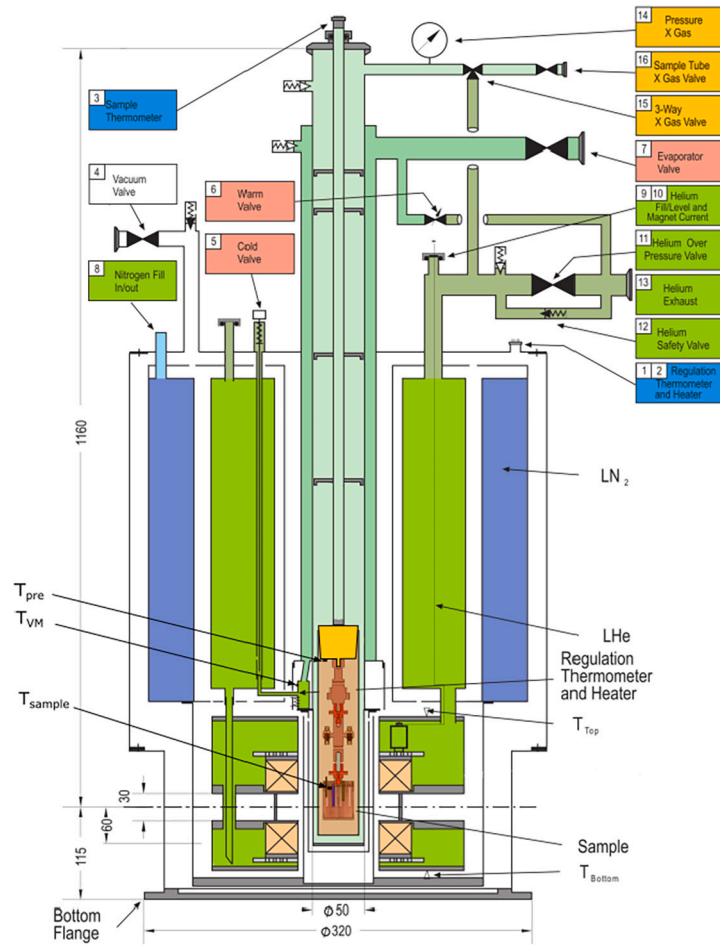


Fig. A.1. Technical drawing of the vertical cryomagnet [39] with overlay of our experimental stage. As indicated in the main text, the experimental stage is enclosed by an aluminum cap and kept in vacuum.

Table A.1

Experimental parameters as used during the course of *B*-sweep experiments. The table shows mean values for sample heater power and the temperatures probed at various positions at the experimental stage.

MeasurementID	Sample Heater Power [μ W]	T_{sample} [K]	T_{pre} [K]	T_{VM} [K]	$T_{pre} - T_{VM}$ [K]	$T_{sample} - T_{pre}$ [K]
0	252	30.0	25.04	20.18	4.86	4.96
1	252	30.0	24.99	20.32	4.67	5.01
2	127	30.0	25.01	20.03	4.98	4.99
3	71	30.0	25.0	20.12	4.88	5.0
4	36	30.0	25.0	20.32	4.68	5.0
5	0	30.0	25.0	20.19	4.81	5.0
6	202	30.0	25.0	20.06	4.94	5.0
7	202	30.0	25.0	20.3	4.7	5.0
8	202	30.0	25.0	20.06	4.94	5.0
9	202	30.0	25.0	20.02	4.98	5.0
10	207	22.0	16.0	13.0	3.0	6.0
11	105	22.0	16.0	13.0	3.0	6.0
12	201	32.5	28.5	25.0	3.5	4.0
13	199	37.5	33.5	31.09	2.41	4.0
14	198	40.0	36.0	33.5	2.5	4.0
15	197	42.5	38.5	36.0	2.5	4.0
16	202	30.0	27.0	25.0	2.0	3.0
17	201	32.5	29.5	27.5	2.0	3.0
18	200	35.0	32.0	30.0	2.0	3.0
19	199	37.5	34.5	32.5	2.0	3.0
20	198	40.0	37.0	35.0	2.0	3.0
21	197	42.5	39.49	36.87	2.62	3.01
22	196	45.0	41.99	39.81	2.18	3.01
23	195	47.5	44.49	42.3	2.19	3.01
24	195	50.0	46.99	43.99	3.0	3.01
25	193	55.0	51.98	48.08	3.9	3.02
26	192	60.0	56.98	53.33	3.65	3.02
27	204	27.0	21.0	19.0	2.0	6.0
28	203	28.0	22.0	20.0	2.0	6.0
29	202	29.0	23.0	21.0	2.0	6.0

A.2. Cable and device assignments

Table A.2

Pin assignment of the 24-pin Fischer connector, connected devices and cable materials.

pins & channel	function	cable materials
1-4 (CH1)	not used	constantan
5-8 (CH2)	T_{pre} -sensor	constantan + phosphor bronze
9-12 (CH3)	T_{sample} -sensor	constantan + phosphor bronze
13-16 (CH4)	15 k Ω sample heater	constantan+ manganin+ phosphor bronze
17-20 (CH5)	not used	constantan
20-21 (CH6)	heater pre-stage (2p)	copper
22-24 (CH6)	heater sample stage (2p)	copper

Table A.3

Monitored temperatures and their corresponding temperature controllers and control loops. The monitored temperatures include the cryo-magnet temperatures, T_{top} and T_{bottom} (Fig. A.1) and room temperature T_{room} .

device	temperature	PI looped output	controlled device
LS340 (1)	T_{VM}	Output 1	VTI-heater
LS340 (1)	T_{top}	—	—
LS340 (2)	T_{rack}	Analog	rack fans
LS340 (2)	T_{room}	—	—
LS350	T_{pre}	Output 1	heater pre-stage
LS350	T_{sample}	Output 2	heater sample stage
LS350	T_{bottom}	—	—

A.3. Measurement data excerpts

Fig. A.3 shows a four-day long data excerpt with data channels for T_{sample} (T_{THE_holder}), T_{pre} ($T_{Prestage}$), T_{VM} ($T_{VM3-VTI}$), the He level, the capacitances of thermometers T1 and T2 (C1 and C2), the B field and the converted temperatures T1 and T2. Two Helium fillings were performed during this time, which is in agreement with the stand time of the cryostat. The temperature stability is increased for every stage towards the sample (compare T_{VM} , T_{pre} and T_{sample}). As seen in the center of Fig. A.3 T_{sample} stays within less than 500 μ K during He filling while T_{VM} changes by about 5 K. Fig. A.3 also indicates different B field sweep types by showing three sawtooth like and one linear sweep. Finally, low temperature noise is seen for channels T1 and T2 for zero-field parts. A slight temporal drift is observed in this long term study.

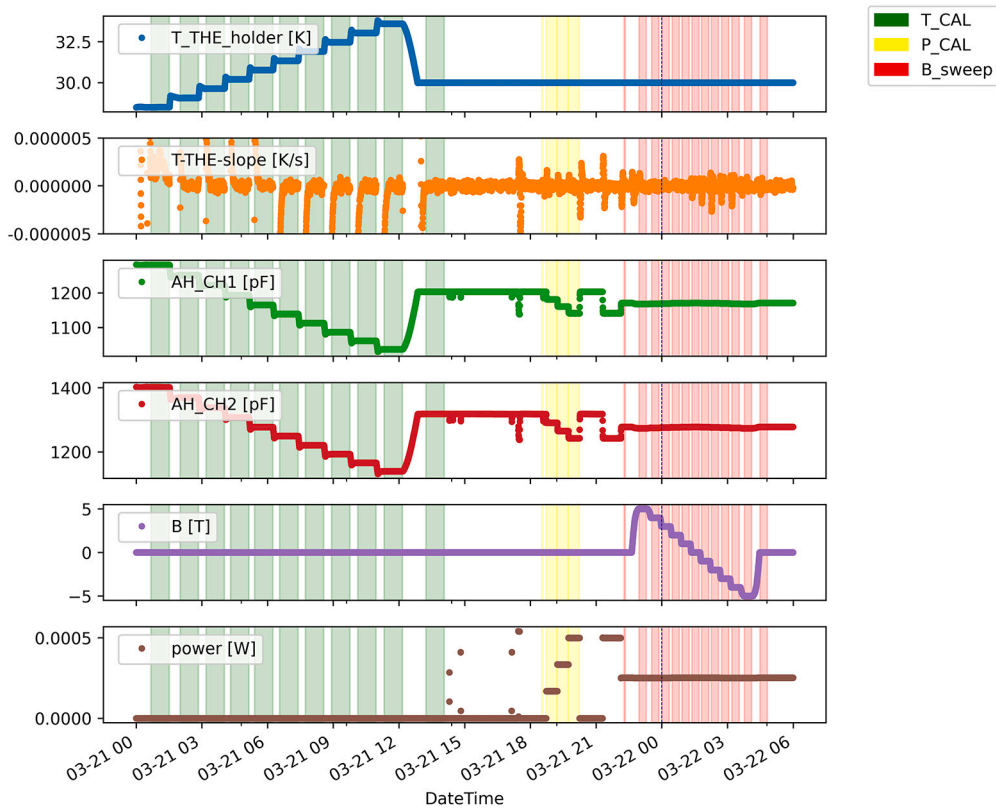


Fig. A.2. Visualization of the different measurement modes for temperature calibration (T_{CAL} , $B = 0$, $P = 0$, green background), power calibration/thermal conductivity measurement (P_{CAL} , $T_{sample} = const.$, $B = 0$, yellow background) and a B -field sweep (B_{sweep} , $T_{sample} = const.$, $P = const.$, pink background).

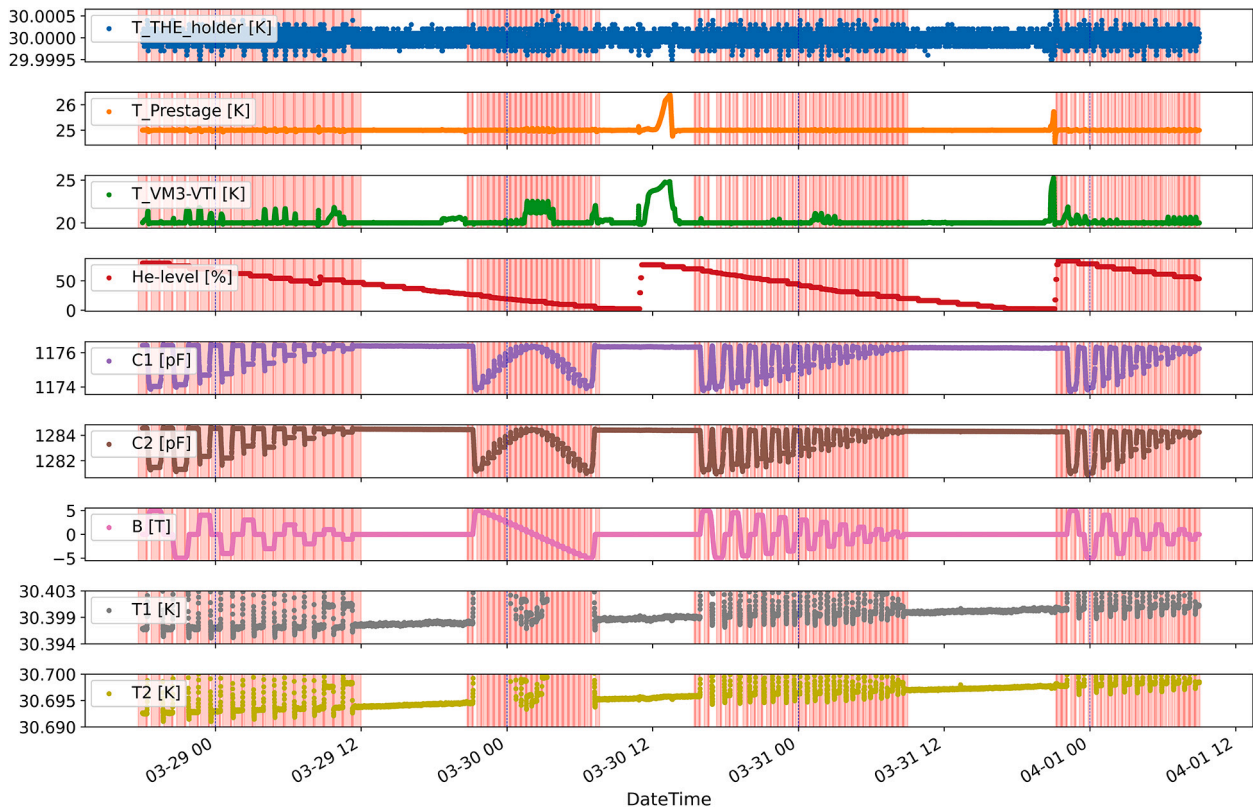


Fig. A.3. A four-day excerpt from the logged data confirms the independence of the sample thermometers from previous stages and visualizes the different *B*-sweep types. The pink marked regions indicate measurement times at stabilized conditions.

A.4. Temperature calibration

In our experiment *in situ* measured capacitance as function of temperature is used to calibrate the capacitance thermometers by means of non-linear least square fitting. However, previously reported models result in moderate deviations, so that we applied a set of different fitting models (Table A.4) and check for their quality by evaluation of the relative and absolute deviation with respect to the given data points.

Table A.4

Models used to fit temperature calibration data. *x* is the free parameter that represents either capacitance or temperature.

Fit model	Equation
Curie-Weiss	$\frac{C}{x - T_c}$
Curie-Weiss modified	$\epsilon_0 + \frac{C}{x - T_c M}$
Barretts	$\left(\frac{T_1}{2} \cdot \frac{\cosh\left(\frac{T_1}{2x}\right)}{\sinh\left(\frac{T_1}{2x}\right)} - T_0 \right)$
hyperbolic	$\frac{A}{B \cdot \frac{\cosh\left(\frac{B}{x}\right)}{\sinh\left(\frac{B}{x}\right)} - C}$
linear inverse	$A + Bx + Cx^{-1}$
linear inverse quadratic	$A + Bx + Cx^{-1} + Dx^2 + Ex^{-2}$
pole-pole	$A + \frac{B}{x - C} + \left(\frac{D}{x - E}\right)^2$
rational poly3	$\frac{AC - \frac{x}{B} - Cx}{A + Bx + Cx^2 + Dx^3} + Dx + Ex^2 + Fx^3$
rational function	$\frac{A - x}{1 + Ex + Fx^2}$
poly _{<i>n</i>}	$\sum_{i=0}^n A_i x^i$
log_poly _{<i>n</i>}	$10^{\sum_{i=0}^n A_i \log_{10}(x)^i}$

We considered both manual and automatic selection for the data points included in the fitting procedure. For the manual approach, we selected data sets where a distinct temperature calibration was performed manually and sets of thermal conductivity measurements where the heating power was zero. The set of these points refers to “T_CAL” in the Figs. A.4, A.9 and A.11.

For the automatic selection, we consider data points with zero B field and zero power ($< 1 \times 10^{-10}$ W). We further filter the data based on the rolling slope of the sample holder temperature T_{sample} and capacity over the previous 20 measurement points, which represents approximately 4 min. The filter criteria are given in the comments column of Table A.5. We name the selected regions using the following scheme: T[3,4]_P[3,4], where the number in square brackets represents the order of the threshold value for sample holder temperature change and capacity change, respectively. To ensure comparability between fits for different raw data point selections and to minimize the indirect weighting of the fit due to the number of points, we implemented temperature binning with 400 bins to equalize the distribution of data points.

Table A.5
Region names and corresponding number of points.

Region name	Number of points before binning	Comments
T_CAL	5161	based on temperature calibrations and power calibrations with $P = 0$
T3_P2	48191	$\partial T_{sample}/\partial t < 1 \times 10^{-3} \text{ K s}^{-1}$, $\partial C_{[1,2,3]}/\partial t < 1 \times 10^{-2} \text{ F s}^{-1}$, $T \leq 200 \text{ K}$
T4_P3	30822	$\partial T_{sample}/\partial t < 1 \times 10^{-4} \text{ K s}^{-1}$, $\partial C_{[1,2,3]}/\partial t < 1 \times 10^{-3} \text{ F s}^{-1}$, $T \leq 200 \text{ K}$
T4_P4	24745	$\partial T_{sample}/\partial t < 1 \times 10^{-4} \text{ K s}^{-1}$, $\partial C_{[1,2,3]}/\partial t < 1 \times 10^{-4} \text{ F s}^{-1}$, $T \leq 200 \text{ K}$
T4_P5	14074	$\partial T_{sample}/\partial t < 1 \times 10^{-4} \text{ K s}^{-1}$, $\partial C_{[1,2,3]}/\partial t < 3 \times 10^{-5} \text{ F s}^{-1}$, $T \leq 200 \text{ K}$

We conducted non-linear least square fitting on all combinations of previously mentioned regions and functions listed in Table A.4. Polynomials were applied up to the ninth order and logarithmic polynomials up to seventh order. These limits are set to reduce over fitting. We considered to fit capacitance $C(T)$ as well as temperature $T(C)$. This two-fold strategy is driven by the physical motivation behind fitting $C(T)$ and the computational efficiency of applying a $T(C)$ fit for temperature evaluations. To evaluate the quality of our fits, we determined the maximum absolute and relative deviation for each model, resulting in four distinct categories. The graphical results are presented in Fig. A.4. To analyze the effect of different possible decisions during the data analysis, we made a selection of fitted regions. Therefore, in each category we selected five sets with the lowest deviations and merged these selections. The maximum absolute and relative deviations of these selections for the three thermometers are summarized in Table A.6. These individual selections were used to calibrate the thermometers and to calculate the final results. The deviations of each fit are also shown for individual thermometers as a function of temperature in Figs. A.5 and A.6. Dashed lines indicate that the fits exhibit low deviations within the temperature range where the THE measurements were performed.

To ensure transparency and a well-documented data pipeline, we solely utilized Python and its common packages (e.g., lmfit, pandas, numpy, matplotlib) within Jupyter Lab notebooks for processing raw data and generating the final images. For the computationally intensive fitting processes, parallel computing was employed for reducing processing times.

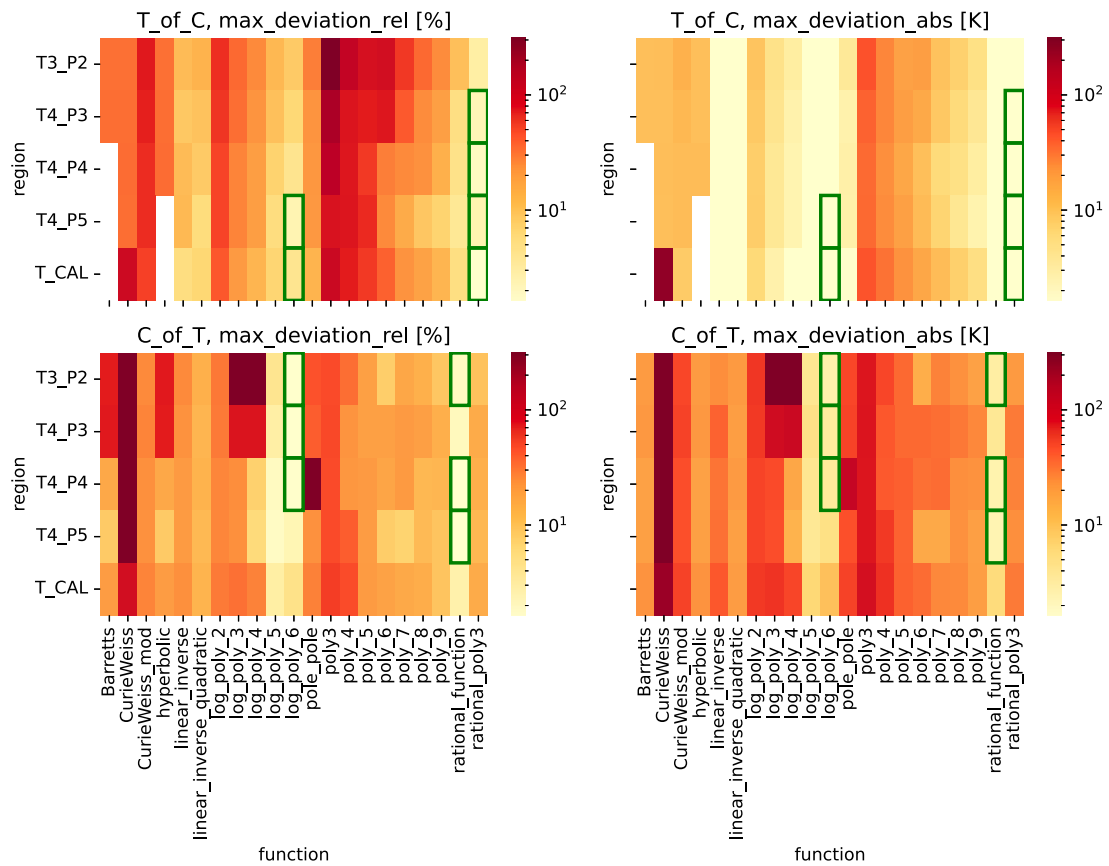


Fig. A.4. Heatmap showing the maximum absolute deviation and maximum relative deviation obtained from various fit models listed in Table A.4 and raw data selections listed in Table A.5 applied to the $T(C)$ and $C(T)$ data representation. The five values with lowest deviations in each category are marked by a green rectangle. These selected models were further used to calibrate the thermometers and calculate averaged results. White regions represent region/model combinations for which the fits did not converge.

Table A.6

Selection of fit results showing the maximum absolute and relative deviation for three thermometers. Values are sorted by the sum of absolute and relative deviation.

Region	Function	Fit_type	max_deviation_abs [K]	max_deviation_rel [%]
T_CAL	rational_poly3	T(C)	0.634	1.643
T4_P4	rational_poly3	T(C)	0.530	1.974
T4_P3	rational_poly3	T(C)	0.614	2.295
T4_P5	log_poly_6	T(C)	0.564	2.451
T4_P5	rational_poly3	T(C)	0.576	2.503
T4_P5	rational_function	C(T)	2.458	1.203
T4_P4	rational_function	C(T)	2.623	1.348
T3_P2	log_poly_6	C(T)	2.710	1.421
T_CAL	log_poly_6	T(C)	0.611	4.073
T4_P3	log_poly_6	C(T)	3.336	1.627
T3_P2	rational_function	C(T)	3.065	2.001
T4_P4	log_poly_6	C(T)	3.445	1.680

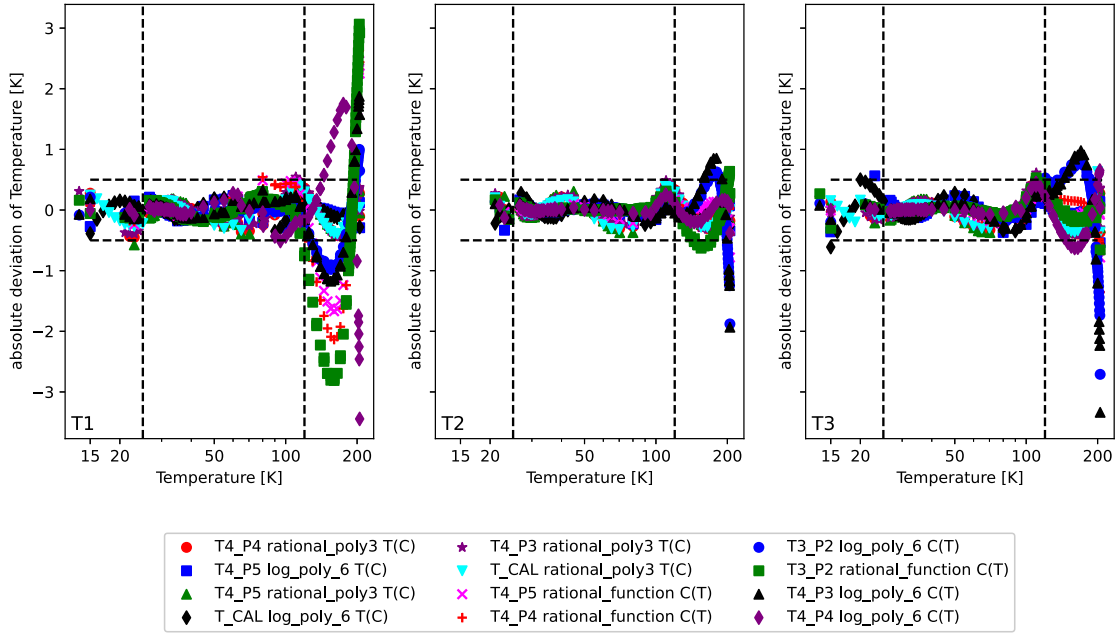


Fig. A.5. Absolute deviation of selected temperature calibration fits.

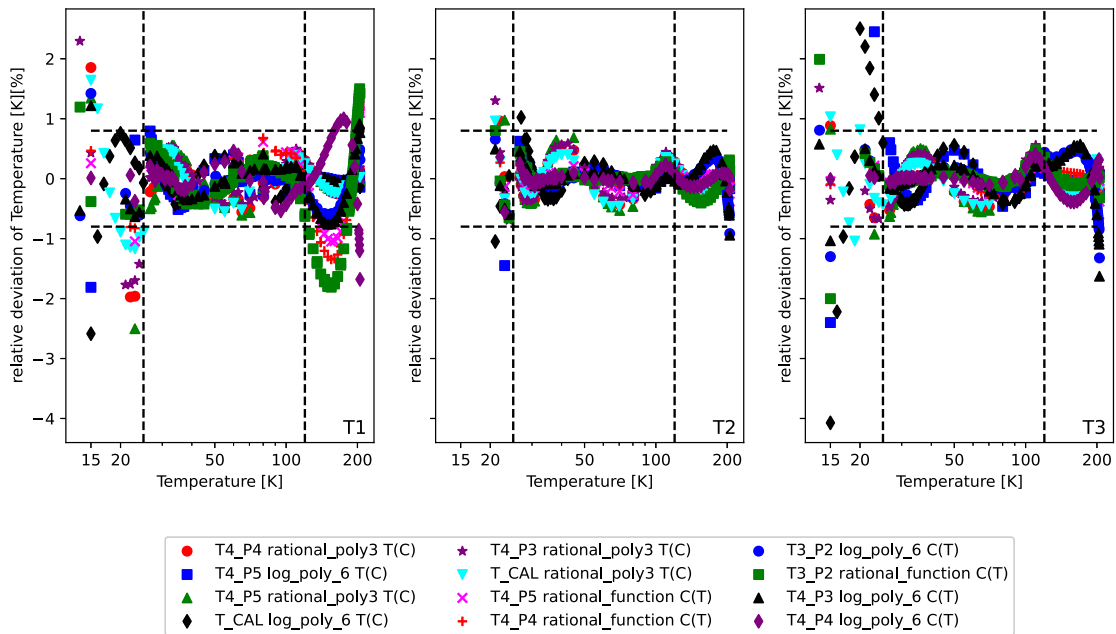


Fig. A.6. Relative deviation of selected temperature calibration fits.

A.5. Field dependence of STO thermometers

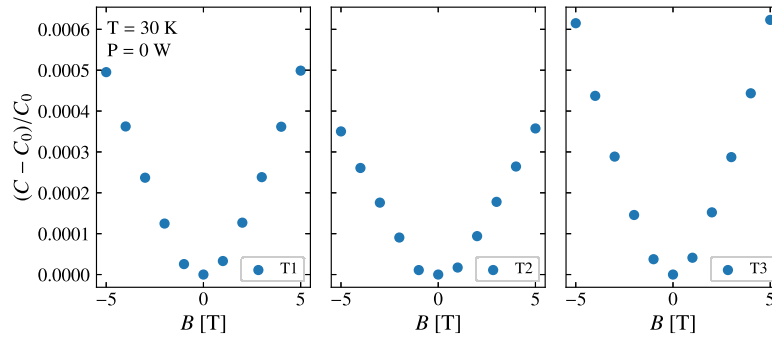


Fig. A.7. Relative capacitance change of three STO thermometers measured at 30 K and zero heating power.

A.6. Longitudinal thermal conductivity $\kappa_{xx}(B, T)$

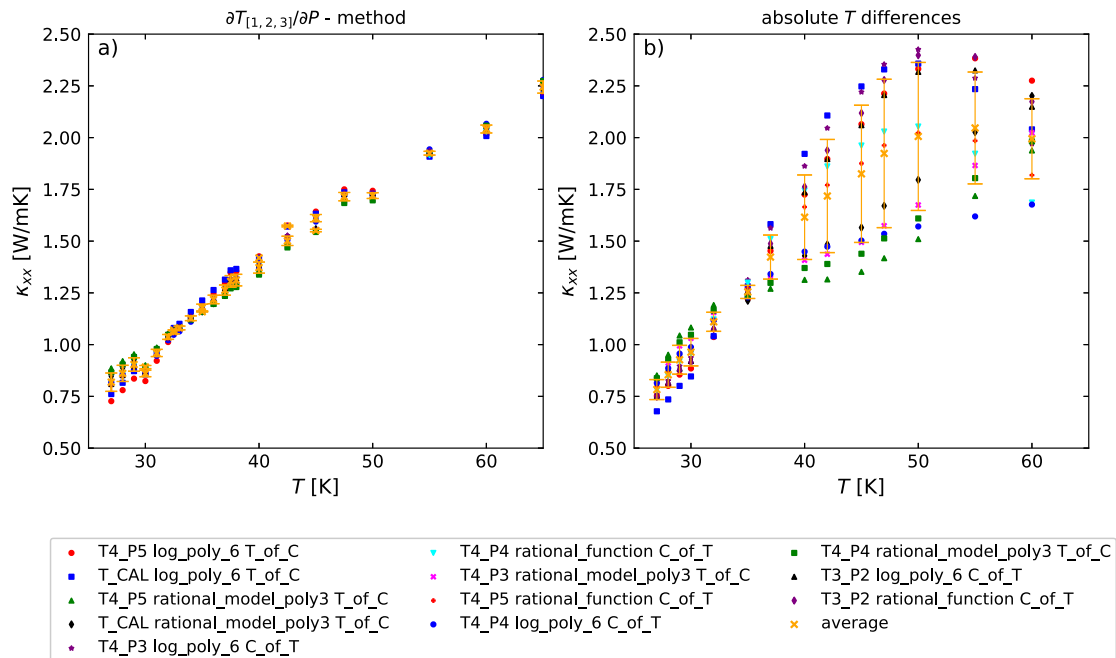


Fig. A.8. Longitudinal thermal conductivity $\kappa_{xx}(T)$ for two analysis methods a) based on the slopes $\partial T_{[1,2,3]}/\partial P$ of power calibrations and b) using absolute temperature differences at fixed power. Different choices of thermometer calibrations are shown.

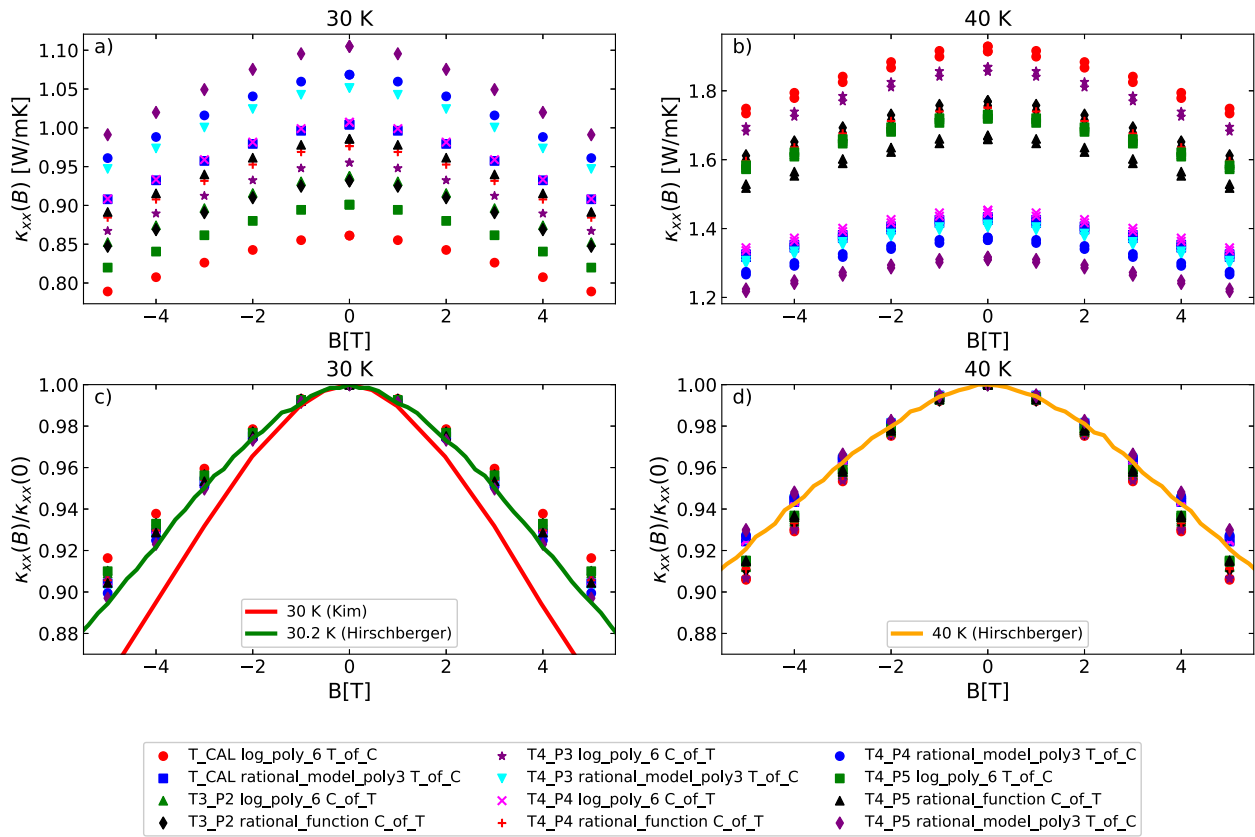


Fig. A.9. a,b) Longitudinal thermal conductivity κ_{xx} shows large deviations for different choices of thermometer calibrations at 30 K and 40 K. c,d) The relative change of the longitudinal thermal conductivity show a maximum error of about 3 % for different choices for the thermometer calibration.

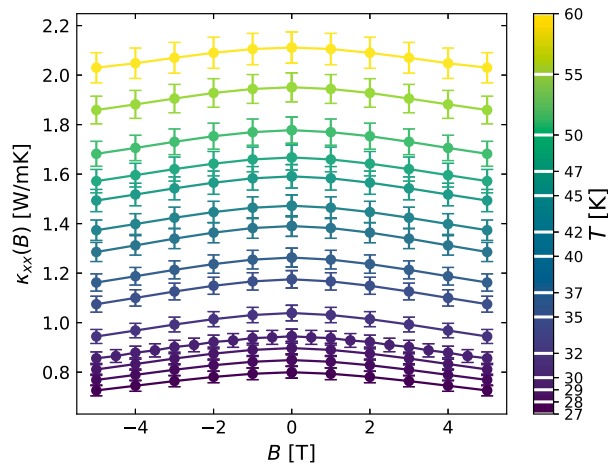


Fig. A.10. Longitudinal thermal conductivity κ_{xx} as function of B . Relative changes with respect to B of the set ‘T_CAL rational_model_poly3 T_of_C’ were multiplied with $\kappa_{xx}(B = 0)$ from power calibrations. Error bars indicate the 3 % error from the choice of the thermometer calibration.

A.7. Transverse temperature differences

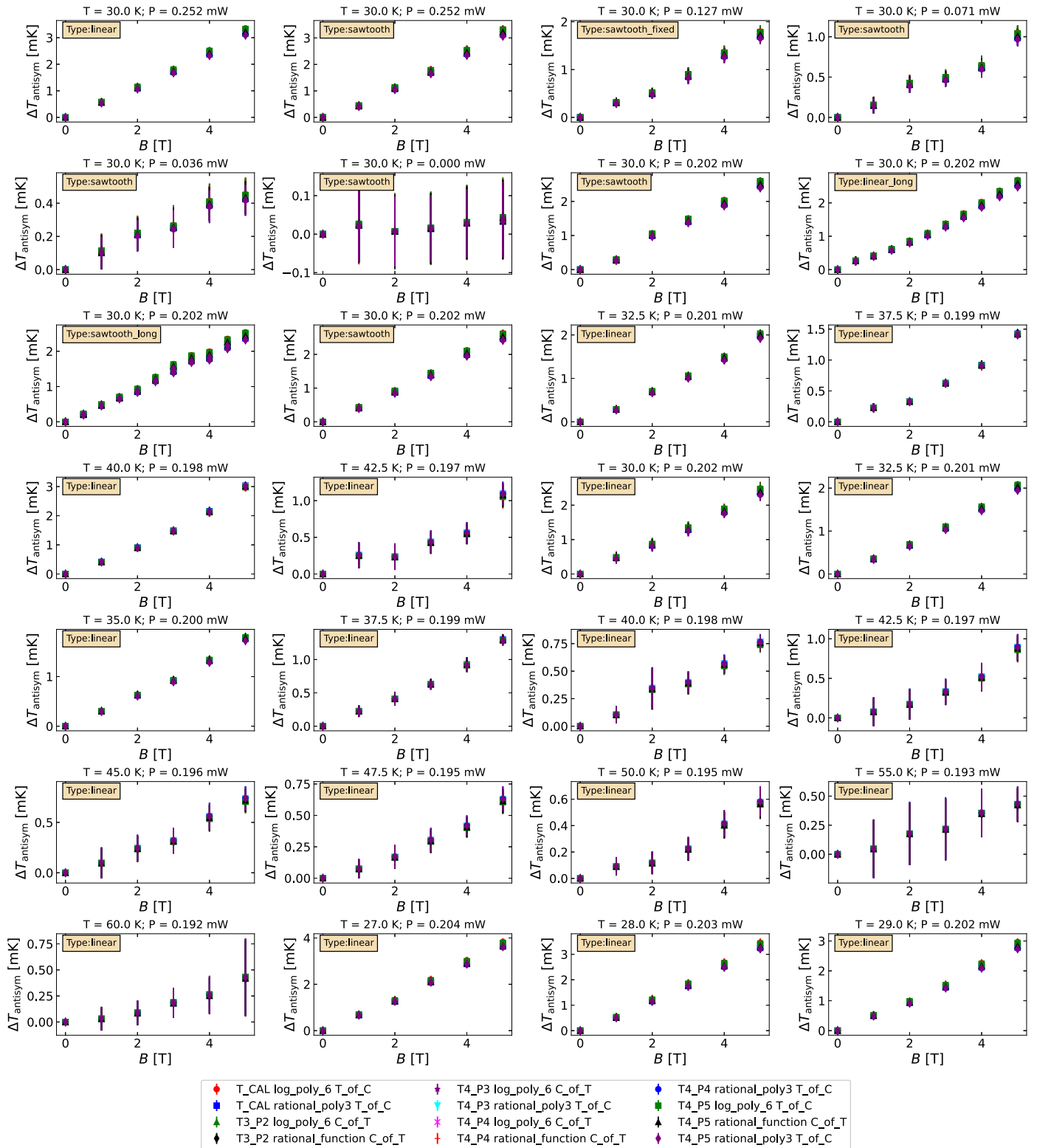


Fig. A.11. A set of anti-symmetrized transverse temperature differences was analyzed for different base temperatures, applied sample powers, sweep types, and thermometer calibrations. Uncertainties are based on Eq. (7).

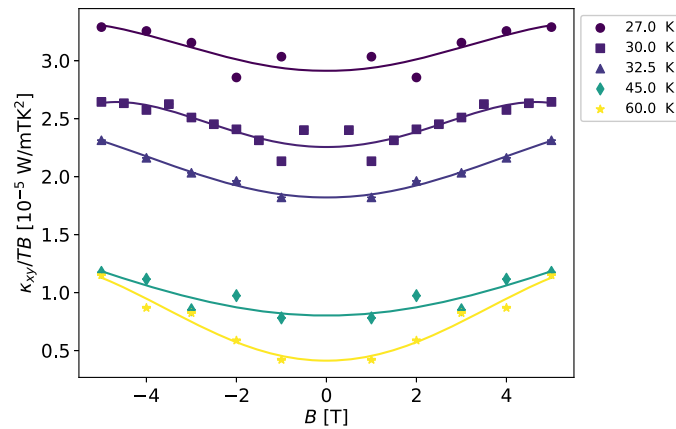
A.8. Transverse thermal conductivity κ_{xy} 

Fig. A.12. Calculated field and entropy reduced transverse thermal conductivity fitted with a fourth-order polynomial for the data set ‘T_CAL rational_model_poly3 T_of_C’. Error bars include the propagated uncertainty of $\kappa_{xx}(B=0)$ determined by Eq. (5) and the uncertainty of the relative longitudinal thermal conductivity for different thermometer calibration selections.

References

- [1] M. Hirschberger, J.W. Krizan, R.J. Cava, N.P. Ong, Large thermal Hall conductivity of neutral spin excitations in a frustrated quantum magnet, *Science* 348 (6230) (2015) 106–109, <https://doi.org/10.1126/science.1257340>, <https://www.science.org/doi/pdf/10.1126/science.1257340>, <https://www.science.org/doi/abs/10.1126/science.1257340>.
- [2] T. Uehara, T. Ohtsuki, M. Udagawa, S. Nakatsuji, Y. Machida, Phonon thermal Hall effect in a metallic spin ice, *Nat. Commun.* 13 (1) (2022) 4604, <https://doi.org/10.1038/s41467-022-32375-0>.
- [3] Y. Zhang, N.P. Ong, P.W. Anderson, D.A. Bonn, R. Liang, W.N. Hardy, Giant enhancement of the thermal Hall conductivity κ_{xy} in the superconductor $\text{YBa}_2\text{Cu}_3\text{O}_7$, *Phys. Rev. Lett.* 86 (2001) 890–893, <https://doi.org/10.1103/PhysRevLett.86.890>, <https://link.aps.org/doi/10.1103/PhysRevLett.86.890>.
- [4] X. Li, B. Fauqué, Z. Zhu, K. Behnia, Phonon thermal Hall effect in strontium titanate, *Phys. Rev. Lett.* 124 (2020) 105901, <https://doi.org/10.1103/PhysRevLett.124.105901>, <https://link.aps.org/doi/10.1103/PhysRevLett.124.105901>.
- [5] H. Takagi, T. Takayama, G. Jackeli, G. Khalilullin, S.E. Nagler, Concept and realization of Kitaev quantum spin liquids, *Nat. Rev. Phys.* 1 (4) (2019) 264–280, <https://doi.org/10.1038/s42254-019-0038-2>.
- [6] Y. Kasahara, T. Ohnishi, Y. Mizukami, O. Tanaka, S. Ma, K. Sugii, N. Kurita, H. Tanaka, J. Nasu, Y. Motome, T. Shibauchi, Y. Matsuda, Majorana quantization and half-integer thermal quantum Hall effect in a Kitaev spin liquid, *Nature* 559 (7713) (2018) 227–231, <https://doi.org/10.1038/s41586-018-0274-0>.
- [7] J.A.N. Bruin, R.R. Claus, Y. Matsumoto, N. Kurita, H. Tanaka, H. Takagi, Robustness of the thermal Hall effect close to half-quantization in $\alpha\text{-RuCl}_3$, *Nat. Phys.* 18 (4) (2022) 401–405, <https://doi.org/10.1038/s41567-021-01501-y>.
- [8] H. Li, T.T. Zhang, A. Said, G. Fabbri, D.G. Mazzone, J.Q. Yan, D. Mandrus, G.B. Halász, S. Okamoto, S. Murakami, M.P.M. Dean, H.N. Lee, H. Miao, Giant phonon anomalies in the proximate Kitaev quantum spin liquid $\alpha\text{-RuCl}_3$, *Nat. Commun.* 12 (1) (2021) 3513, <https://doi.org/10.1038/s41467-021-23826-1>.
- [9] É. Lefrançois, G. Grissonnanche, J. Baglo, P. Lampen-Kelley, J.-Q. Yan, C. Balz, D. Mandrus, S. Nagler, S. Kim, Y.-J. Kim, N. Doiron-Leyraud, L. Taillefer, Evidence of a phonon Hall effect in the Kitaev spin liquid candidate $\alpha\text{-RuCl}_3$, *Phys. Rev. X* 12 (2) (2022) 21025, <https://doi.org/10.1103/PhysRevX.12.021025>, <https://link.aps.org/doi/10.1103/PhysRevX.12.021025>.
- [10] S. Li, S. Okamoto, Thermal Hall effect in the Kitaev-Heisenberg system with spin-phonon coupling, *Phys. Rev. B* 106 (2) (2022) 24413, <https://doi.org/10.1103/PhysRevB.106.024413>, <https://link.aps.org/doi/10.1103/PhysRevB.106.024413>.
- [11] P. Czajka, T. Gao, M. Hirschberger, P. Lampen-Kelley, A. Banerjee, N. Quirk, D.G. Mandrus, S.E. Nagler, N.P. Ong, Planar thermal Hall effect of topological bosons in the Kitaev magnet $\alpha\text{-RuCl}_3$, *Nat. Mater.* 22 (1) (2023) 36–41, <https://doi.org/10.1038/s41563-022-01397-w>.
- [12] M.-E. Boulanger, G.e. Grissonnanche, S. Badoux, A. Allaire, E. Lefrançois, A.e. Legros, A. Gourgout, M. Dion, C.H. Wang, X.H. Chen, R. Liang, W.N. Hardy, D.A. Bonn, L. Taillefer, Thermal Hall conductivity in the cuprate Mott insulators Nd_2CuO_4 and $\text{Sr}_2\text{CuO}_2\text{Cl}_2$, *Nat. Commun.* 11 (1) (2020) 5325, <https://doi.org/10.1038/s41467-020-18881-z>.
- [13] X. Li, Y. Machida, A. Subedi, Z. Zhu, L. Li, K. Behnia, The phonon thermal Hall angle in black phosphorus, *Nat. Commun.* 14 (1) (2023) 1027, <https://doi.org/10.1038/s41467-023-36750-3>.
- [14] S. Sim, H. Yang, H.-L. Kim, M.J. Coak, M. Itoh, Y. Noda, J.-G. Park, Sizable suppression of thermal Hall effect upon isotopic substitution in SrTiO_3 , *Phys. Rev. Lett.* 126 (2021) 015901, <https://doi.org/10.1103/PhysRevLett.126.015901>, <https://link.aps.org/doi/10.1103/PhysRevLett.126.015901>.
- [15] S. Jiang, X. Li, B. Fauqué, K. Behnia, Phonon drag thermal Hall effect in metallic strontium titanate, *Proc. Natl. Acad. Sci.* 119 (35) (2022) e2201975119, <https://doi.org/10.1073/pnas.2201975119>, <https://doi.org/10.1073/pnas.2201975119>.
- [16] T. Qin, J. Zhou, J. Shi, Berry curvature and the phonon Hall effect, *Phys. Rev. B* 86 (10) (2012) 104305, <https://doi.org/10.1103/PhysRevB.86.104305>, <https://link.aps.org/doi/10.1103/PhysRevB.86.104305>.
- [17] J.-Y. Chen, S.A. Kivelson, X.-Q. Sun, Enhanced thermal Hall effect in nearly ferroelectric insulators, *Phys. Rev. Lett.* 124 (16) (2020) 167601, <https://doi.org/10.1103/PhysRevLett.124.167601>, <https://link.aps.org/doi/10.1103/PhysRevLett.124.167601>.
- [18] H. Guo, S. Sachdev, Extrinsic phonon thermal Hall transport from Hall viscosity, *Phys. Rev. B* 103 (20) (2021) 205115, <https://doi.org/10.1103/PhysRevB.103.205115>, <https://link.aps.org/doi/10.1103/PhysRevB.103.205115>.
- [19] K. Sun, Z. Gao, J.-S. Wang, Phonon Hall effect with first-principles calculations, *Phys. Rev. B* 103 (21) (2021) 214301, <https://doi.org/10.1103/PhysRevB.103.214301>, <https://link.aps.org/doi/10.1103/PhysRevB.103.214301>.
- [20] R.R. Neumann, A. Mook, J. Henk, I. Mertig, Thermal Hall effect of magnons in collinear antiferromagnetic insulators: signatures of magnetic and topological phase transitions, *Phys. Rev. Lett.* 128 (2022) 117201, <https://doi.org/10.1103/PhysRevLett.128.117201>, <https://link.aps.org/doi/10.1103/PhysRevLett.128.117201>.
- [21] S.K. Kim, K. Nakata, D. Loss, Y. Tserkovnyak, Tunable magnonic thermal Hall effect in skyrmion crystal phases of ferrimagnets, *Phys. Rev. Lett.* 122 (2019) 057204, <https://doi.org/10.1103/PhysRevLett.122.057204>, <https://link.aps.org/doi/10.1103/PhysRevLett.122.057204>.
- [22] G. Grissonnanche, A. Legros, S. Badoux, E. Lefrançois, V. Zatkó, M. Lizaere, F. Laliberté, A. Gourgout, J.-S. Zhou, S. Pyon, T. Takayama, H. Takagi, S. Ono, N. Doiron-Leyraud, L. Taillefer, Giant thermal Hall conductivity in the pseudogap phase of cuprate superconductors, *Nature* 571 (7765) (2019) 376–380, <https://doi.org/10.1038/s41586-019-1375-0>.
- [23] C. Strohm, Magneto-transverse phonon transport, Ph.D. thesis, Universität Konstanz, Germany, 2003.
- [24] G. Grissonnanche, Une fable de phases en interaction dans les cuprates supraconducteurs contée par le transport thermique, Ph.D. thesis, Université de Sherbrooke, Québec, Canada, 2016.
- [25] C. Tinsman, G. Li, C. Su, T. Asaba, B. Lawson, F. Yu, L. Li, Probing the thermal Hall effect using miniature capacitive strontium titanate thermometry, *Appl. Phys. Lett.* 108 (26) (2016) 261905, <https://doi.org/10.1063/1.4955069>.
- [26] H.-L. Kim, M.J. Coak, J.C. Baglo, K. Murphy, R.W. Hill, M. Sutherland, M.C. Hatnean, G. Balakrishnan, J.-G. Park, Modular thermal Hall effect measurement setup for fast-turnaround screening of materials over wide temperature range using capacitive thermometry, *Rev. Sci. Instrum.* 90 (10) (2019) 103904, <https://doi.org/10.1063/1.5108512>.
- [27] C. Tinsman, Thermal Hall effect measurements using strontium titanate microthermometers, Ph.D. thesis, University of Michigan, 01.2019.
- [28] G.D. Mahan, Many Particle Physics, third edition, Plenum, New York, 2000.
- [29] S. Krinner, S. Storz, P. Kurpiers, P. Magnard, J. Heinsoo, R. Keller, J. Lütolf, C. Eichler, A. Wallraff, Engineering cryogenic setups for 100-qubit scale superconducting circuit systems, *EPJ Quantum Technol.* 6 (1) (2019) 2, <https://doi.org/10.1140/epjqt/s40507-019-0072-0>.

- [30] F.D. Natterer, F. Patthey, T. Bilgeri, P.R. Forrester, N. Weiss, H. Brune, Upgrade of a low-temperature scanning tunneling microscope for electron-spin resonance, *Rev. Sci. Instrum.* 90 (1) (2019) 013706, <https://doi.org/10.1063/1.5065384>.
- [31] D. Klimm, C. Gugushev, D.J. Kok, M. Naumann, L. Ackermann, D. Rytz, M. Peltz, K. Dupré, M.D. Neumann, A. Kwasniewski, D.G. Schlom, M. Bickermann, Crystal growth and characterization of the pyrochlore $\text{tb}_2\text{ti}_2\text{o}_7$, *CrystEngComm* 19 (2017) 3908–3914, <https://doi.org/10.1039/C7CE00942A>.
- [32] Q.J. Li, Z.Y. Zhao, C. Fan, F.B. Zhang, H.D. Zhou, X. Zhao, X.F. Sun, Phonon-glass-like behavior of magnetic origin in single-crystal $\text{tb}_2\text{ti}_2\text{o}_7$, *Phys. Rev. B* 87 (2013) 214408, <https://doi.org/10.1103/PhysRevB.87.214408>, <https://link.aps.org/doi/10.1103/PhysRevB.87.214408>.
- [33] G. Rupprecht, R.O. Bell, Dielectric constant in paraelectric perovskites, *Phys. Rev.* 135 (1964) A748–A752, <https://doi.org/10.1103/PhysRev.135.A748>, <https://link.aps.org/doi/10.1103/PhysRev.135.A748>.
- [34] E. Sawaguchi, A. Kikuchi, Y. Kadera, Dielectric constant of strontium titanate at low temperatures, *J. Phys. Soc. Jpn.* 17 (10) (1962), <https://doi.org/10.1143/JPSJ.17.1666>, <https://www.osti.gov/biblio/4740639>.
- [35] E.D. Marquardt, J.P. Le, R. Radebaugh, *Cryogenic Material Properties Database*, Springer US, Boston, MA, 2002, pp. 681–687.
- [36] M. Hirschberger, *Quasiparticle excitations with Berry curvature in insulating magnets and Weyl semimetals*, 2017.
- [37] C. Ang, Z. Yu, Dielectric relaxor and ferroelectric relaxor: Bi-doped paraelectric SrTiO_3 , *J. Appl. Phys.* 91 (3) (2002) 1487–1494, <https://doi.org/10.1063/1.1428799>, https://pubs.aip.org/aip/jap/article-pdf/91/3/1487/10619701/1487_1_online.pdf.
- [38] R. Fletcher, A.J. Friedman, M.J. Stott, The right-lead and Hall coefficients of the noble metals, *J. Phys. F, Met. Phys.* 2 (4) (1972) 729, <https://doi.org/10.1088/0305-4608/2/4/017>, <https://dx.doi.org/10.1088/0305-4608/2/4/017>.

Further reading

- [39] M. Meissner, Usage of sample environment at BENS technical handbook, https://www.helmholtz-berlin.de/media/media/forschung/wi/sample-environment/use2000_6_handbook_edited_cpc_maerz_2009_dw.pdf. (Accessed 19 August 2022), Online.